This is a repository copy of *Weak persistence of Northwest Pacific anomalous anticyclone during post-El Niño summers in CMIP5 and CMIP6 models*.

White Rose Research Online URL for this paper:
https://eprints.whiterose.ac.uk/217037/

Version: Accepted Version

Article:
Tang, H. orcid.org/0000-0002-2924-0126, Huang, G., Hu, K. et al. (4 more authors) (2023) Weak persistence of Northwest Pacific anomalous anticyclone during post-El Niño summers in CMIP5 and CMIP6 models. Climate Dynamics, 61 (7-8). pp. 3805-3830. ISSN 0930-7575

https://doi.org/10.1007/s00382-023-06772-0

This version of the article has been accepted for publication, after peer review (when applicable) and is subject to Springer Nature's AM terms of use, but is not the Version of Record and does not reflect post-acceptance improvements, or any corrections. The Version of Record is available online at: http://dx.doi.org/10.1007/s00382-023-06772-0

Reuse
Items deposited in White Rose Research Online are protected by copyright, with all rights reserved unless indicated otherwise. They may be downloaded and/or printed for private study, or other acts as permitted by national copyright laws. The publisher or other rights holders may allow further reproduction and re-use of the full text version. This is indicated by the licence information on the White Rose Research Online record for the item.

Takedown
If you consider content in White Rose Research Online to be in breach of UK law, please notify us by emailing eprints@whiterose.ac.uk including the URL of the record and the reason for the withdrawal request.

eprints@whiterose.ac.uk
https://eprints.whiterose.ac.uk/

Weak persistence of Northwest Pacific anomalous anticyclone during post-El Niño summers in CMIP5 and CMIP6 models

Haosu Tang[1,3], Gang Huang[1,3*], Kaiming Hu[1,4*], Wenping Jiang[2], Weichen Tao[1], Ya Wang[1], Hongyu Hou[1,3]

[1]*State key Laboratory of Numerical Modeling for Atmospheric Sciences and Geophysical Fluid Dynamics (LASG) / Center for Monsoon System Research (CMSR), Institute of Atmospheric Physics, Chinese Academy of Sciences, Beijing, China*

[2]*Key Laboratory of Marine Hazards Forecasting, Ministry of Natural Resources / College of Oceanography, Hohai University, Nanjing, China*

[3]*University of Chinese Academy of Sciences, Beijing, China*

[4]*Collaborative Innovation Center on Forecast and Evaluation of Meteorological Disasters (CIC-FEMD), Nanjing University of Information Science & Technology, Nanjing, China*

---

* Corresponding author: hg@mail.iap.ac.cn and hkm@mail.iap.ac.cn

Abstract

An anomalous anticyclone (AAC) recurs over the Indo–Northwest Pacific during post-El Niño summers, regulating climate anomalies in the densely populated South, Southeast, and East Aisa. However, AACs simulated in phase 5/6 of the Coupled Model Intercomparison Project (CMIP5/6) multi-model ensemble mean fail to persist through post-El Niño summers. The present study suggests that this weak persistence bias likely stems from the weakly persistent sea surface temperature (SST) anomalies' gradient between the North Indian Ocean and tropical Western Pacific. On one hand, the simulated North Indian Ocean warming decays faster compared with its observational counterpart due to the weakened cross-equatorial antisymmetric wind patterns and wind–evaporation–SST feedback, which may arise from the deep thermocline bias in the Southwest Indian Ocean in CMIP models. On the other hand, the long-lasting Western Pacific warming bias may be led by the intensified upper-ocean zonal advection feedback and wind–downwelling–SST feedback, which can be further traced back to the Pacific cold tongue bias in CMIP models. Compared with CMIP5 models, CMIP6 models simulate a more realistic Southwest Indian Ocean thermocline dome and equatorial Pacific cold tongue. Therefore, the overall simulation skill in the summertime AAC persistence is improved in CMIP6 than in CMIP5 models. The persistence of AAC is further investigated during post-Eastern Pacific (EP) and Central Pacific (CP) El Niño summers in CMIP models. The simulated AAC displays a remarkable stronger persistence during post-EP El Niño summer compared to its post-CP counterpart. The present study highlights that reducing mean-state biases in climate models may elevate the simulation skills of summertime AAC persistence, thereby enhancing seasonal prediction and future projection skills of Asian summer monsoon.

Keywords: El Niño; anomalous anticyclone; persistence; thermocline; cold tongue bias

1. Introduction

El Niño-Southern Oscillation (ENSO), originating from equatorial central and eastern Pacific, is the dominant mode of climate fluctuation at interannual timescale and exerts far-reaching impacts across the world (e.g., McPhaden et al. 2006; Hu et al. 2021). ENSO is generally phase locked to an annual cycle, which features growth in boreal summer, mature during winter, and fade in the following spring (hereafter seasons denote those of the Northern Hemisphere). A low-level anomalous anticyclone (AAC) anchored to the Indo–Northwest Pacific (NWP) is a recurrent pattern during post-El Niño summers, bridging preceding El Niño with Asian summer monsoon and posing extensive climate impacts on the densely populated South, Southeast, and East Aisa (EA). Specifically, the AAC could transport water vapor from tropical oceans to EA and Indian peninsula through southwesterly winds along its western periphery, inducing heavy rainfall even severe floods via intensifying low-level moisture convergence (Chang et al. 2000; Chowdary et al. 2013; Tang et al. 2022a, b). Meanwhile, the areas cloaked in the ridge of the AAC often suffer from sunny and scorching weathers mainly due to enhanced adiabatic subsidence heating and solar radiation (Hu et al. 2011; Deng et al. 2019). Moreover, the AAC could break the summer NWP monsoon trough, thereby suppressing local tropical cyclone genesis (Du et al. 2011). The AAC is generally considered as the tropical lobe of the Pacific–Japan/East Asia–Pacific (PJ/EAP) teleconnection pattern (Nitta 1987; Huang and Sun 1992). Together with the anomalous cyclonic circulation to its northeast, the AAC spanning the Indo–NWP warm pool can further influence the synoptic weather and climate in the mid-latitude of EA and serve as the principal origin of seasonal predictability for EA summer climate (Kosaka et al. 2013).

As for the formation and maintenance mechanisms of AAC pattern, the El Niño-induced cold sea surface temperature anomalies (SSTA) over tropical NWP can

suppress local convective activities and excite a low-level AAC as the atmospheric Rossby wave response on its northwest side. The AAC further reinforces the NWP cold SSTA via the wind–evaporation–SST (WES) feedback, persisting into El Niño decaying summer (Wang et al. 2000; Li et al. 2017). Nevertheless, the tropical NWP cold SSTA gradually decline with the withdrawal of the northeasterly trade winds during El Niño decaying summer. Therefore, another school of studies indicated that the El Niño-induced Indian Ocean basin (IOB) warming can serve as a capacitor in maintaining the summer AAC pattern via the Kelvin wave-induced surface Ekman divergence mechanism (Xie et al. 2009). These two schools of opinions further evolved into the Indo–western Pacific Ocean capacitor effect, which highlights the roles of both IO and tropical NWP (Kosaka et al. 2013; Xie et al. 2016; Du et al. 2022).

Summer (June to August) is the monsoon season for EA when the rainfall variability exerts immense socioeconomic impacts. Previous studies concerning EA summer rainfall variability mainly focused on the seasonal mean climate diagnosis and assessment. However, summer climate in EA experiences dramatic variations on the sub-seasonal timescale (Ye and Lu 2010; Xiang et al. 2013; Li et al. 2022). For example, summer rain belt in EA is not stagnant but shifts northward gradually, accompanied by the northward jump of western Pacific subtropical high (WPSH) (Tao et al. 1987). These sub-seasonal changes of background mean-states over EA–NWP can further lead to the intensification and northward extension of AAC in post-El Niño mid-summer, whereas the northward shift phase of AAC lags that of background mean-state WPSH (Tang et al. 2021). As a result, the decaying El Niño usually hinders the summer northward jump of WPSH and the concomitant rain belt over EA, exposing the Yangtze River basin to an elongated wet season with diminished sunlight.

Coupled general circulation models (CGCMs) are essential tools in seasonal prediction and future projection. Given the impacts of AAC on weather and climate

anomalies across the Indo–EA, it requires an in-depth assessment of how well the AAC pattern is simulated in the state-of-the-art CGCMs archived in the Coupled Model Intercomparison Project (CMIP). Most CGCMs can capture the general characteristics (i.e., spatial and seasonal features) of the AAC and show relatively high skills in simulating and predicting AAC-related precipitation and temperature anomalies during post-El Niño summers (Chowdary et al. 2010; Kim et al. 2012). Nonetheless, systematic biases (deviations from observations) exist in the detailed properties of the simulated summer AAC. Previous studies indicated that CMIP models suffer from a common underestimation of AAC magnitude during post-El Niño summers. As regards the origins, several studies suggested that the weakened IO capacitor effect and excessive westward extension of El Niño-related SSTA should take responsibility for the weak magnitude bias of the simulated AAC (Tao et al. 2016, 2018, 2019; Jiang et al. 2017; Li et al. 2019).

Previous studies have identified different flavors of El Niño, of which the most widely accepted classification is the Eastern Pacific (EP) and Central Pacific (CP) El Niño (Ashok et al. 2007; Yu and Kim 2013). The maximum SSTA of EP and CP El Niño normally take place in the eastern and central equatorial Pacific, respectively, posing distinct impacts on the weather and climate across the world (Yu et al. 2012). Several studies have indicated that the AAC may respond diversely to two types of El Niño (Chen and Li 2021; Wang et al. 2021). The AAC and its accompanying climate anomalies are generally weaker during post-CP El Niño summers than those during post-EP El Niño summers (Feng et al. 2011; Yuan and Yang 2012; Jiang and Li 2022). Recent studies have examined the performance of ENSO diversity and the associated atmospheric teleconnections and climate phenomena under EP and CP El Niño in CMIP5/6 models (Zou et al. 2014; Xu et al. 2017; Freund et al. 2020). The amplitude and structure of CP El Niño are found better simulated in CMIP6 MME compared with CMIP5 MME (Hou and Tang, 2022), possibly attributed to the reduced mean-state SST

bias in the Niño-4 region (Jiang et al. 2021).

Compared with the seasonal mean magnitude of summertime AAC, its sub-seasonal evolution in CMIP models is less evaluated but of vital realistic significance (Yu et al. 2021). Pioneering studies have implied a poor persistence of AAC during post-El Niño summers in CMIP5 models (Du et al. 2013; Hu et al. 2014). However, the underlying physical mechanisms are not yet adequately clarified and remain a knowledge gap. Therefore, the present study aims to systematically investigate the persistence of summertime AAC and its physical origins in CMIP models at sub-seasonal timescale. Besides, from CMIP5 to CMIP6, CGCMs have become more skillful in reproducing background mean-state conditions over Indo–NWP and capturing sophisticated multiscale interactions inherent in EA monsoon systems (Jiang et al. 2022; Yang and Huang 2022). Thus, we also attempt to probe whether CMIP6 models outperform their CMIP5 counterparts in simulating the persistence of summer AAC, and if so, which physical processes contribute to this performance improvement. Furthermore, the present study will also examine the simulations of AAC persistence during post-EP and post-CP El Niño summers in CMIP models, in an effort to provide insights into the climate impacts induced by ENSO diversity.

The remaining paper is organized as follows. Section 2 describes the data and methods. Section 3 presents a full picture of the biased persistence of summer AAC in CMIP5 and CMIP6 models. A hierarchy of physical mechanisms contributing to the model biases is investigated in Section 4. Section 5 provides discussions on the diverse responses of AAC persistence during the post-CP and post-EP El Niño summers in CMIP models. The high-performance CMIP models are also selected in this section, followed by a summary in Section 6.

2. Data and methods

2.1 Data

148 The observational datasets include the monthly Hadley Centre Sea Ice and SST
149 (HadISST) dataset (Rayner et al. 2003), Climate Prediction Center Merged Analysis of
150 Precipitation (CMAP) dataset (Xie and Arkin 1997), and the National Centers for
151 Environmental Prediction–National Center for Atmospheric Research (NCEP–NCAR)
152 atmospheric reanalysis (Kalnay et al. 1996) for 1979–2005. We also use the monthly
153 Simple Ocean Data Assimilation ocean/sea ice reanalysis (SODA) ocean state variables,
154 i.e., subsurface potential temperature and ocean current velocity, for the period 1979–
155 2005 (Carton and Giese 2008).

156 The monthly outputs for 1979–2005 from 36 CMIP5 (Taylor et al. 2012) and 45
157 CMIP6 (Eyring et al. 2016) models are adopted in the present study (Table 1). Here, we
158 analyze only the first ensemble member (commonly, 'r1i1p1' for CMIP5 and 'r1i1p1f1'
159 for CMIP6) of the historical run of each model. The main conclusions of this study are
160 generally robust against extended study period (i.e., 1979–2014) and varying model
161 numbers. For consistency, all the observations and model simulations are horizontally
162 interpolated onto 2.5° × 2.5° grids using bilinear interpolation before analysis. In the
163 vertical direction, the observed and simulated oceanic variables are linearly interpolated
164 into the common 82 levels from 10 m to 4800 m.

165 *2.2 Methods*

166 *2.21 Definition of climate indices*

167 We employ D(0)JF(1) Niño-3.4 index to track ENSO variability, which is defined as
168 the SSTA averaged over the central-eastern Pacific (5°S–5°N, 120°W–170°W). Here,
169 suffix 0 and 1 in parentheses refer to ENSO year and its post year, respectively. We
170 define the El Niño years as those when the standardized D(0)JF(1) Niño-3.4 indices are
171 above 0.5. Ten El Niño events (namely 1982/83, 1986/87, 1987/88, 1991/92,1994/95,
172 1997/98, 2002/03, 2004/05, 2006/07 and 2009/10) are identified for further study
173 (Supplementary Table 1). Since we concentrate on El Niño-induced interannual

174 variability, we subtract the 11-yr running mean from the original datasets before
175 analysis to eliminate decadal or longer variations. The cold tongue index (CTI), defined
176 as the regional-averaged mean-state SST over the equatorial Pacific cold tongue area
177 (3°S–3°N, 150°E–140°W), is introduced to delineate the equatorial cold tongue bias.
178 The cold tongue is more westward-extended in the model with lower CTI. We use the
179 probability density function (PDF) to depict the likelihood of CTI in CMIP5 and CMIP6
180 models. Through observing the horizontal shift of PDF, one can judge whether CTI
181 changes significantly under two generations of CMIP models. The kernel density
182 estimation is adopted to fit CTI at monthly scales, which is a non-parametric technique
183 for the PDF estimation of an assigned dataset. The 95% uncertainty ranges (2.5th to
184 97.5th percentiles) of CTI in CMIP models are estimated via the bootstrapping
185 resampling test (Tang et al. 2022a). Specifically, we compute the 95% uncertainty
186 ranges of CMIP5 and CMIP6 MME by 10000 random samplings (with replacement),
187 respectively. The CMIP6 MME is considered statistically distinct from CMIP5 MME
188 only when CMIP6 MME is not included in the 95% uncertainty ranges of CMIP5
189 (Planton et al. 2021).

190 We define the thermocline depth as that of the 20°C isotherm. The focus of the
191 present study is on post-El Niño summer, i.e., June(1), July(1) and August(1), which is
192 the monsoon season for EA when the IO capacitor comes into effect (Wu et al. 2009;
193 Chen et al. 2016). The composite of SST, precipitation, surface air temperature (SAT),
194 atmospheric and oceanic circulation anomalies during post-El Niño summers are used
195 to represent El Niño-induced variabilities. We also repeat our analyses but regress
196 climate variables against the standardized D(0)JF(1) Niño-3.4 index to examine the
197 results. The multi-model ensemble mean (MME) is calculated as the average of model
198 outputs with equivalent weights, which reflects the overall performance of CMIP
199 models. If more than 80% of models agree with the sign of the MME, we deem it as a
200 statistically significant inter-model agreement. We calculate the statistical significances

of composite and regression analyses based on two-sided Student's t-test.

2.22 Three criteria to distinguish EP and CP El Niño events

Considering the robustness of El Niño behaviors may be sensitively affected by the events captured, we adopt three criteria in the present study to distinguish EP and CP El Niño events and compare the composite results. First, we adopt the classification criteria based on D(0)JF(1) Niño-3 (5°S–5°N, 150°W–90°W) and Niño-4 (5°S–5°N, 160°E–150°W) indices to select EP and CP El Niño events (Yeh et al. 2009). An EP (CP) El Niño event is defined when the D(0)JF(1) Niño-3 index is greater (less) than the Niño-4 index. Second, we classify EP and CP El Niño events via the El Niño Modoki index (EMI; Ashok et al. 2007), that is:

$$EMI = [SSTA]_A - 0.5 \times [SSTA]_B - 0.5 \times [SSTA]_C \quad (1)$$

where $[SSTA]_A$, $[SSTA]_B$, and $[SSTA]_C$ indicate regional-mean SSTA over region A (10°S–10°N, 165° E–140°W), region B (15°S–5°N, 110–70°W) and region C (10°S–20°N, 125–145°E), respectively. A CP El Niño event is identified when the EMI is greater than or equal to 0.8σ (standard deviation). Third, the cold tongue Niño index (Niño_{CT}) and warm pool Niño index (Niño_{WP}) are employed to quantify the two types of El Niño quantitatively (Ren and Jin 2011), which are piecewise linear combinations of Niño-3 and Niño-4 indices:

$$\begin{cases} \text{Niño}_{\text{CT}} = \text{Niño3} - \alpha\text{Niño4} \\ \text{Niño}_{\text{WP}} = \text{Niño4} - \alpha\text{Niño3} \end{cases}, \quad \alpha = \begin{cases} 0.4, \text{Niño3} \times \text{Niño4} > 0 \\ 0, \text{Niño3} \times \text{Niño4} \le 0 \end{cases} \quad (2)$$

The El Niño events with Niño_{WP} greater (less) than Niño_{CT} are defined as CP (EP) El Niño events. The selection results in the observation, CMIP5 and CMIP6 models based on three criteria are summarized in the Supplementary Tables 1, 2 and 3.

2.23 Diagnostic tools

To assess the energy propagation of PJ teleconnection pattern, the horizonal wave-

activity fluxes (Takaya and Nakamura 2001) are defined as:

$$W = \frac{1}{2|\vec{V}|}\begin{Bmatrix} \bar{U}(\psi_x'^2 - \psi'\psi'_{xx}) + \bar{V}(\psi'_x\psi'_y - \psi'\psi'_{xy}) \\ \bar{U}\left(\psi'_x\psi'_y - \psi'\psi'_{xy}\right) + \bar{V}\left(\psi_y'^2 - \psi'\psi'_{yy}\right) \end{Bmatrix} \quad (3)$$

where $\vec{V}$ is the horizontal wind velocity vector, U and V denote the zonal and meridional wind velocity, respectively. ψ represents the geostrophic stream function. The primes and overbars represent the composite anomalies during post-El Niño summers and background mean-state quantities, respectively.

To illuminate the physical processes underlying SSTA changes, we employ the upper-ocean heat budget (e.g., Xie et al. 2010; Chen et al. 2016) as:

$$\partial T'/\partial t = \frac{Q'}{\rho C_p h} - \bar{u}\frac{\partial T'}{\partial x} - u'\frac{\partial \bar{T}}{\partial x} - \bar{v}\frac{\partial T'}{\partial y} - v'\frac{\partial \bar{T}}{\partial y} - \bar{w}\frac{\partial T'}{\partial z} - w'\frac{\partial \bar{T}}{\partial z} + D \quad (4)$$

in which the prime indicates the composite anomaly and the overbar represents the background mean-state quantity. T and $\partial T/\partial t$ denote the oceanic potential temperature and its tendency, respectively. Q represents the net ocean–atmosphere heat flux including latent heat flux, sensible heat flux, net surface shortwave radiation and net surface longwave radiation (positive value indicates downward surface heat flux, i.e., ocean warming). ρ $(= 10^3 kg \cdot m^{-3})$ is the seawater density, C_p $(= 4000J \cdot kg^{-1} \cdot K^{-1})$ is the ocean specific heat capacity, and h is the thickness of the ocean mixed layer. h is taken as a constant 50 m in the present study, and the analysis results are not sensitive to different thicknesses of ocean mixed layer, i.e., 30 m or 70 m. $u, v,$ and w denote ocean current velocity in three dimensions. Since CMIP5 models did not provide w, we only examine the contributions of w-related terms in CMIP6 models. D is the diffusion term. The nonlinear terms are omitted due to trivial influence in this study.

3. Weak persistence of AAC and its climate impacts

Figure 1 illustrates the composite monthly 850-hPa wind and precipitation anomalies from June(1) to August(1) in the observations, CMIP5 and CMIP6 MME. The AAC hovering over the Indo–NWP warm pool and its concomitant precipitation response can persist throughout post-El Niño summers in the observations (Figs. 1A, 1D and 1G). Both CMIP5 and CMIP6 MME can capture the general characteristics of the AAC pattern in the post-El Niño early summer (Figs. 1B, 1C, 1E and 1F). However, the AAC shifts eastward away from the mainland and fails to maintain over EA in August(1) in CMIP5 and CMIP6 MME (Figs. 1H and 1I). Similar results can be obtained from the regression analyses (Supplementary Figs. 1G, 1H and 1I) and extended time period (Supplementary Figs. 2E and 2F). We further evaluate each CMIP model individually and find this weak persistence of the simulated summer AAC might be a common model bias (figures not shown).

The observational El Niño-induced precipitation anomalies display a meridional dipole pattern over EA during post-El Niño summer: rainfall is reduced over the NWP, while enhanced along the Meiyu/Baiu front. Subject to the weak persistence of AAC, the anomalous rain belt extending from the southern part of East China to Korea and South Japan disappears in August(1) in CMIP5 and CMIP6 MME (Figs. 1H and 1I), exhibiting distinct discrepancies from the observation. Similar results could be obtained from the regression analyses (Supplementary Figs. 1G, 1H and 1I). This simulation failure may potentially lead to a limited skill and substantial inter-model uncertainty in the prediction of EA summer monsoon in late summer compared with early summer months. Figure 2 displays the composite monthly 850-hPa wind and SAT anomalies from June(1) to August(1) in the observations, CMIP5 and CMIP6 MME. We observe the above-normal SAT anomalies in South China and Indo–China peninsula accompanied by AAC in August(1) in the observations (Fig. 2G). However, the anomalous SAT patterns are vastly diminished in August(1) in CMIP5 and CMIP6 MME (Figs. 2H and 2I). Similar phenomenon can be observed from the regression

analyses (Supplementary Figs. 3G, 3H and 3I).

We further diagnose the energy propagation of PJ pattern from June(1) to August(1) in the observations, CMIP5 and CMIP6 MME. The low-level poleward energy propagations over tropical NWP are relatively weaker in CMIP models in August(1) compared with their observational counterpart (Supplementary Figs. 4G, 4H and 4I). To quantitatively depict the monthly evolutions of summer AAC, we define the AAC index as the difference of 850-hPa zonal winds between a northern region (20°–30°N, 110°–140°E) and a southern region (5°–15°N, 100°–130°E) (Wang and Fan 1999; Jiang et al. 2017). In the observations, the AAC intensity is stronger in July(1) and August(1) than in June(1) (Tang et al. 2021). Nevertheless, the AAC persists weakly in CMIP5 and CMIP6 MME, indicating that CMIP models fail to reproduce the evolution of summertime AAC (Fig. 3). This weak persistence bias will further lead to the weak magnitude bias of summer mean AAC. CMIP6 MME simulates a more realistic AAC evolution than its CMIP5 counterpart during post-El Niño summer, albeit still at relatively low level. We also use another AAC index, i.e., regional-averaged 850-hPa relative vorticity anomalies over the tropical NWP (10°–35°N, 120°–160°E; Wu et al. 2010). The conclusion remains robust against different AAC index definitions (Supplementary Fig. 5). In the next section, we will investigate the role of SSTA in each ocean basin to comprehend the physical origins of the biased persistence of AAC in more detail.

4. Physical mechanisms

4.1 Weak persistence of NIO–WP SSTA gradient

Figure 4 demonstrates the composite monthly SSTA from June(1) to August(1) in the observations, CMIP5 and CMIP6 MME. The SSTA in the IO feature IOB warming throughout post-El Niño summer in the observations (Figs. 4A, 4D and 4G). The IOB warming patterns in CMIP5 and CMIP6 MME are comparable to the observations in

301 the post-El Niño early summer (Figs. 4B, 4C, 4E and 4F). However, they are
302 significantly weaker than those in the observational August(1), indicating a weak
303 persistence of IOB warming (Figs. 4H and 4I). In addition, the equatorial Pacific
304 decaying El Niño-related SSTA penetrate too far westward in CMIP5 and CMIP6 MME
305 than their observational counterpart, and could persist over the tropical west Pacific
306 (WP) during the entire post-El Niño summer. The above two SSTA biases can be
307 observed from the regression analyses (Supplementary Fig. 6) and extended time period
308 (Supplementary Fig. 7) as well.

309 Following previous studies (Ohba and Ueda 2006; He and Zhou 2015; Jiang et al.
310 2017, 2019), we construct the inter-basin SSTA gradient index as SSTA differences
311 between North IO (NIO; 0°–20°N, 50°–120°E) and WP (10°S–10°N, 140°E–170°W).
312 Figure 5 shows the monthly evolutions of NIO–WP SSTA gradient in the observations,
313 CMIP5 and CMIP6 models. Due to the rapidly decaying IOB warming and long-lasting
314 WP warming bias during post-El Niño summers, the NIO–WP SSTA gradients persist
315 weakly in CMIP5 and CMIP6 MME compared with their observational counterpart.
316 The SSTA gradient is relatively better simulated in CMIP6 MME than in CMIP5 MME,
317 corresponding to the performance improvement of summer AAC. To confirm the
318 relationship between AAC index and NIO–WP SSTA gradient, the corresponding
319 scatterplots from June(1) to August(1) are displayed in Figure 6. The AAC magnitudes
320 are correlated with NIO warming throughout post-El Niño summers, with relatively
321 high inter-model correlations of 0.41, 0.32 and 0.43 in June(1), July(1) and August(1),
322 respectively ($n = 83,\ p < 0.01$). In addition, the AAC magnitudes are negatively
323 associated with the unrealistic WP warming from June(1) to August(1), indicating that
324 the model with stronger WP warming bias tend to reproduce weaker AAC during post-
325 El Niño summers. Their inter-model correlations are -0.34, -0.61 and -0.65 in June(1),
326 July(1) and August(1), respectively ($n = 83,\ p < 0.01$). The stronger correlations
327 indicate that the long-lasting WP warming bias may play a more important role than the

328 weakly persistent NIO warming in discontinuing the AAC persistence in post-El Niño
329 late summers. The inter-model correlation coefficients between AAC index and NIO–
330 WP SSTA gradient further improve, reaching 0.57, 0.73 and 0.75 in June(1), July(1)
331 and August(1), respectively ($n = 83,\ p < 0.01$). It connotes that the simulated NIO–
332 WP SSTA gradient may be the key factor of the inter-model spread of AAC magnitude
333 during post-El Niño summer months.

334 How does the NIO–WP SSTA gradient affect the lower-level AAC during post-El
335 Niño summers? Figure 7 presents the composite monthly 200-hPa wind and
336 geopotential height anomalies from June(1) to August(1) in the observations, CMIP5
337 and CMIP6 MME. In the observations, the 200-hPa geopotential height anomalies, as
338 the proxy of tropospheric temperature anomalies, display a Matsuno–Gill (Matsuno
339 1966; Gill 1980) pattern over the tropical IO throughout post-El Niño summer. The
340 atmospheric warm Kelvin waves along the equator penetrate into WP, with upper-level
341 westerly anomalies dominating over the Maritime Continent (Figs. 7A, 7D and 7G).
342 Nevertheless, the unrealistic warm SSTA in WP in CMIP models can strengthen the
343 local convection/rainfall activities and induce upper-level easterly anomalies on the
344 western side, resulting in weak upper-level wind responses over the Maritime Continent
345 (Figs. 7H and 7I). This phenomenon can also be observed from the regression analyses
346 (Supplementary Fig. 8H and 8I). In the lower troposphere, an anomalous cyclonic
347 circulation emerges over the tropical NWP as the Rossby wave response to unrealistic
348 WP warming bias (Figs. 1H and 1I). The WP warming-induced westward spreading
349 atmospheric Rossby wave will attenuate the NIO warming-induced eastward
350 propagating equatorial Kelvin wave. The weakening extent is possibly determined by
351 the NIO–WP SSTA gradient. Therefore, the weakly persistent NIO–WP SSTA gradient
352 may finally result in the weak persistence of AAC during post-El Niño summers in
353 CMIP5 and CMIP6 models.

Apart from the influence of SSTA gradient, the NWP mean-state changes also play a critical role in the sub-seasonal evolution of summer AAC (Xiang et al. 2013; Hu et al. 2019). Supplementary Figure 9 shows the mean-state precipitation over EA–NWP from June to August in the observations, CMIP5 and CMIP6 MME. In general, the CMIP models could reasonably reproduce the onset and eastward advance of mean-state NWP summer monsoon, albeit with relatively weak magnitudes. As indicated by Xie et al. (2009), the extent to which the SSTA can influence NWP circulation anomalies depends on the NWP background mean-state precipitation. The models with stronger mean-state NWP precipitation tend to reproduce intensified moist feedback between local convection and circulation anomalies, thereby enhancing AAC patterns. Hence, even though the SSTA weakens slightly from post-El Niño early to late summer, AAC can still intensify in the observation (Fig. 3). This intensification can be partly attributed to the onset of background NWP summer monsoon in the late summer, which results in enhanced condensational heating anomalies (Wu et al. 2010; Tang et al. 2021). Here, we regress the 850-hPa wind and precipitation onto the standardized AAC index in each grid point to quantify the local moist/convection–circulation feedback (Fig. 8). We define the moist feedback intensity as the regional-mean regressed precipitation anomalies over the key region of moist feedback (10°–20°N, 120°–150°E). The moist feedback intensity shows a generally good relationship with NWP background mean-state precipitation, consistent with previous studies (Wang et al. 2021). However, we also note that the increase of moist feedback intensity from early to late summer is weaker in CMIP5 and CMIP6 MME compared with the observation (Figs. 8D, 8H and 8L), which can be attributed to the weaker onset the simulated NWP summer monsoon (Supplementary Fig. 9). The result still holds when we slightly enlarge or shrink the chosen region. Therefore, the weakened increase of moist/convection–circulation feedback intensity may not be able to provide enough support for the intensification of AAC in August(1) in CMIP models as that in the observation. To further probe the

relative contributions of SSTA gradient and local mean-state changes, the scatter diagram between AAC index and moist feedback intensity is given (Supplementary Fig. 10). The poorly simulated relationship in the post-El Niño late summer implies a much more important contribution of the decaying NIO–WP SSTA gradient than that of the weakened increase of moist feedback to the biased persistence of summer AAC in CMIP models.

4.2 Weak persistence of IOB warming

Figure 9 presents the longitude–time section of 0–20°N averaged El Niño-related SSTA and 850-hPa wind anomalies in the IO in the observations, CMIP5 MME, CMIP6 MME, as well as their corresponding differences. The IOB warming is generally less persistent during post-El Niño summers in CMIP5 and CMIP6 MME compared with the observation (Figs. 9D and 9E). We also observe an overall improvement in IOB warming simulation in CMIP6 MME relative to the CMIP5 MME (Fig. 9F). Why does the IOB warming in CMIP5 and CMIP6 MME could not persist into post-El Niño late summer? Figure 10 exhibits the contributions of latent heat flux, sensible heat flux, shortwave radiation, and longwave radiation anomalies to NIO warming. In the observation, the anomalous latent heat flux and shortwave radiation play the more important roles than the other two terms in NIO warming during post-El Niño spring and summer (Figs. 10A, 10D, 10G, and 10J), consistent with previous studies (Tao et al. 2016). However, the simulated positive latent heat flux and shortwave radiation anomalies could not persist into post-El Niño late summer (Figs. 10B, 10C, 10H, and 10I), resulting in the less persistent IOB warming. The contributions of the oceanic dynamic terms (four oceanic horizontal advection terms) to NIO warming are relatively small (Supplementary Fig. 11).

To further probe the cause of less persistent positive latent heat flux anomalies in CMIP models, the time–latitude section of 40°–100°E averaged El Niño-related

407 precipitation and wind anomalies in the observations, CMIP5 and CMIP6 MME are
408 shown in Figure 11. The observational precipitation anomalies exhibit wet (dry) center
409 south (north) of the equator during post-El Niño spring, accompanied by the cross-
410 equatorial C-shaped wind anomalies (Fig. 11A). The northern branch of the C-shaped
411 wind anomalies over NIO could persist into subsequent summer seasons, which plays
412 a key role in the persistence of positive latent heat flux anomalies (Wu et al. 2008; Du
413 et al. 2009). However, the cross-equatorial antisymmetric spring wind patterns are
414 poorly captured in the CMIP5 and CMIP6 MME (Figs. 11D and 11E). How do the
415 cross-equatorial antisymmetric wind patterns form and why are they weakly simulated
416 in CMIP models? In the observation, the El Niño–induced anomalous anticyclonic
417 circulations in the southeast IO trigger downwelling oceanic Rossby waves propagating
418 westward in D(0)JF(1). The Rossby waves reach the tropical Southwest IO (SWIO;
419 10°S–5°S, 50°E–80°E) after one season where the shallow background thermocline
420 dome locates. As a result, the local thermocline is deepened, further leading to the
421 SWIO warming during post-El Niño spring (Xie et al. 2002). The SWIO positive SSTA-
422 induced rainfall anomalies excite the cross-equatorial antisymmetric wind pattern
423 during post-El Niño spring, the northern branch of which (i.e., anomalous northeasterly)
424 favors NIO warming after the background mean-state southwesterly monsoon onset in
425 May through the WES feedback (Du et al. 2009). Finally, the observational IOB
426 warming can persist through the entire post-El Niño summer (Fig. 4G).

427 Nevertheless, CMIP models suffer from the deeper background mean-state SWIO
428 thermocline depths. Specifically, the regional-mean SWIO thermocline depth during
429 spring (March to May) is only 83.25 m in the observations, whereas it reaches 101.63
430 m in CMIP5 MME and 98.41 m in CMIP6 MME (Fig. 12). Previous studies indicated
431 that the oceanic Rossby wave-induced thermocline disturbance could hardly affect the
432 SSTA when the background mean-state thermocline is deep (Li et al. 2015; Zheng et al.
433 2016). In that case, the deepened thermocline-induced SWIO rainfall anomalies in

CMIP models will become weak. Thus, the deep thermocline bias in CMIP models may finally result in drying (wetting) bias with weaker northwesterly (northeasterly) wind anomalies in the southern (northern) equatorial IO (Figs. 11B and 11C). The dampened wind anomalies, especially the northeasterly wind anomalies north of the equator, further lead to the weak persistence of positive latent heat flux anomalies via the weakened WES feedback (Figs. 10B and 10C).

Where does the deep thermocline bias in CMIP models originate from? Previous studies have indicated that the CGCMs normally suffer from the so-called IO Dipole-like biases, which feature annual mean easterly wind biases on the equator (Lee et al. 2013; Li et al. 2015; Zheng et al. 2016). The mean-state surface winds in the equatorial IO play an important role in the establishment of the thermocline dome in the SWIO. The model with stronger (weaker) background westerly wind along the equator tends to reproduce strengthened (weakened) surface cyclonic wind curls and upwelling Ekman pumping, thereby a shoaling (deepening) SWIO thermocline dome. Therefore, the mean-state equatorial easterly wind biases result in the deep thermocline biases in the SWIO, finally leading to a less persistent IOB warming.

In addition to the cross-equatorial C-shaped wind-anchored IOB warming, the inter-basin positive feedback between IOB warming and AAC pattern is also crucial to the maintenance of IOB warming (Kosaka et al. 2013; Xie et al. 2016). In the observations, the easterly anomalies on the southern periphery of AAC extend westward to NIO in August(1). They will relax the mean-state southwesterly monsoon and suppress surface evaporation, which is instrumental in surface warming over NIO and south China sea (Fig. 10A). Moreover, the AAC can reduce cloud amount and enhance insolation over Bay of Bengal and the northern south China sea, contributing to the local warming (Fig. 10G). The enhanced IOB warming can in turn strengthen the AAC via the IO capacitor effect, forming the positive feedback. Nevertheless, the simulated AAC spanning the

Indo–NWP warm pool decouples with IOB warming in August(1) in CMIP models. This decoupling finally results in the vanishment of additional NIO warming (Figs. 10B, 10C, 10H and 10I).

4.3 Long-lasting WP warming bias

Figure 13 shows the longitude–time section of 10°S–10°N averaged El Niño-related SSTA and wind anomalies over the Pacific in the observations, CMIP5 MME, CMIP6 MME, and their corresponding differences. The differences between CMIP5/6 MME and observations exhibit a long-lasting positive warming center over equatorial WP, known as the excessively westward-extended El Niño-related warming bias (Figs. 13D and 13E). We also note a reduced excessive westward extension of WP warming bias in CMIP6 MME compared with their CMIP5 counterparts during post-El Niño summer (Fig. 13F). To further illustrate the origins of the long-lasting WP warming bias, we first conduct a diagnostic analysis on sea surface heat flux (Fig. 14). We find that the El Niño warming-induced negative latent heat flux and shortwave radiation anomalies are detrimental to the maintenance of positive SSTA, whereas positive longwave radiation anomalies may not be able to hold the balance. We also note that the simulated shortwave radiation anomalies are more westward-extended compared with their observational counterpart, possibly because that the mean-state SST in the warm pool region is higher and easier to trigger convection anomalies. To sum up, thermodynamic processes (i.e., sea surface heat flux anomalies) alone could not explain this long-lasting WP warming bias throughout post-El Niño summers. The oceanic dynamical processes may be vitally important for the artificial equatorial WP warming during post-El Niño summers in CMIP models (Tao et al. 2018; Jiang et al. 2021).

Figure 15 presents the background mean-state SST averaged from June to August in the observations, CMIP5 and CMIP6 MME in the tropical Pacific. In the observations, the tropical equatorial Pacific features a zonally asymmetric pattern with a cold tongue

(warm pool) in the east (west) (Fig. 15A). However, the simulated equatorial cold tongue is too cold and too far westward-extended, known as the equatorial Pacific zonal SST bias (hereafter cold tongue bias) in CMIP models (Figs. 15B and 15C). The strong persistence of cold tongue bias may be traced back to the misrepresentation of tropical ocean–atmosphere interaction in the Pacific Ocean (Li and Xie 2014). The regional-mean CTI during summer is 28.56 °C in the observations, whereas it drops to 27.98 and 28.02 °C in CMIP5 and CMIP6 MME, respectively. Relative to CMIP5 models, we observe a slight warming shift and less diversity of CTI PDF in CMIP6 models (Fig. 15D). This indicates a general reduction of the cold tongue bias over WP in CMIP6 models than in CMIP5 models (Grose et al. 2020; Jiang et al. 2021). Nevertheless, this improvement cannot pass the bootstrap resampling test since the 95% uncertainty ranges of CMIP5 encompass CMIP6 MME. Therefore, we infer that the summer cold tongue bias improvement may not be statistically significant from CMIP5 to CMIP6, consistent with Planton et al. (2021).

Previous studies suggested that models with stronger cold tongue bias tend to displace westward the simulated El Niño-related warming pattern along the equatorial Pacific (Jiang et al. 2021). The scatter diagram of summer CTI versus JJA(1) WP warming bias among CMIP models also indicates a generally good relationship between them (Fig. 15E). To shed light on the physical linkages between equatorial Pacific mean-state cold tongue bias and strong persistence of spurious WP SSTA, the ocean dynamic processes are introduced. Figure 16 demonstrates four horizontal oceanic advection terms in the upper-ocean heat budget. From the heat budget aspect, we observe the artificial warming during post-El Niño summers due to two oceanic zonal advection terms in CMIP models. First, the excessive westward extension of simulated El Niño-related positive SSTA can enhance the horizontal SSTA gradient $(-\partial T'/\partial x)$ over the equatorial WP. Thus, the mean-state zonal warm advection

512 ($-\bar{u}\,\partial T'/\partial x$) will bring about a more westward-extended El Niño-related warming
513 pattern in CMIP models (Figs. 16B and 16C). Second, the mean-state horizontal SST
514 gradient ($-\partial\bar{T}/\partial x$) over the equatorial WP is enhanced possibly due to the cold tongue
515 bias in CMIP models. Therefore, the anomalous eastward ocean current on the equator
516 could lead to a stronger anomalous zonal warm advection ($-u'\,\partial\bar{T}/\partial x$), favoring SST
517 warming over the equatorial WP and forming zonal advection feedback during post-El
518 Niño summers (Figs. 16H and 16I). Besides, we also observe a notable equatorial
519 Pacific warming bias induced by the mean meridional advection of anomalous
520 temperature gradient ($-\bar{v}\,\partial T'/\partial y$) during post-El Niño summers (Figs. 16E and 16F).
521 The meridional SSTA gradient ($-\partial T'/\partial y$) over the equatorial WP may be related with
522 westward-extended positive SSTA as well. The contributions from the anomalous
523 meridional advection of mean temperature gradient ($-v'\,\partial\bar{T}/\partial y$) are relatively small
524 (Figs. 16K and 16L). Similar conclusions can be obtained via the regression analysis
525 (Supplementary Fig. 12). In addition, previous studies suggested that the contribution
526 of mean vertical advection of anomalous potential temperature gradient ($-\bar{w}\,\partial T'/\partial z$),
527 known as thermocline feedback, is also of vital importance during the post-El Niño
528 summer (Kug et al. 2010; Chen and Li 2021). Therefore, we further investigate the
529 potential contributions of thermocline feedback ($-\bar{\omega}\,\partial T'/\partial z$) and upwelling feedback
530 ($-\omega'\,\partial\bar{T}/\partial z$) to equatorial WP warming bias (Fig. 17). The thermocline feedback and
531 upwelling feedback are generally well captured in CMIP6 models and may not be the
532 main causes for the long-lasting WP warming bias.

533 From the oceanic fluctuation view, the westerly wind bias emerges on the equatorial
534 WP during post-El Niño summer in CMIP models (Figs. 13D and 13E), which may be
535 related to the weak persistence of simulated summer AAC. This westerly wind bias
536 could trigger the downwelling ocean Kelvin waves that propagate eastward and help
537 maintain the El Niño. The artificial persistence of El Niño in the simulations (Fig. 4)
538 can lead to the equatorial WP warming bias, which may in turn undermine the AAC

539 persistence and form wind–downwelling–SST feedback.

540 **5. Discussions**

541 In this section, we further examine the persistence of AAC during post-EP and post-
542 CP El Niño summers. All the three criteria have the ability to distinguish two types of
543 El Niño during El Niño developing winter (Supplementary Figs. 13, 14, 15). Figure 18
544 illustrates the composite monthly 850-hPa wind and precipitation anomalies during
545 post-EP and post-CP El Niño summers (identified with Niño-3 and Niño-4 index) in the
546 observations, CMIP5 and CMIP6 MME. The observational AAC and rainfall anomalies
547 during post-EP El Niño summers bear notable similarities with those during entire post-
548 El Niño summers (Figs. 18A, 18D and 18G). Besides, we find a slight improved
549 simulation skill of AAC persistence during post-EP El Niño late summer compared with
550 the entire post-El Niño late summer in CMIP models (Figs. 18H and 18I). The
551 composite results during post-CP El Niño summers differ from those in post-EP El Niño
552 summers. Specifically, the observational AAC and precipitation anomalies are weak
553 and loosely organized during post-CP El Niño summers (Figs. 18J, 18M and 18P). In
554 CMIP models, the simulated AAC and precipitation anomalies are weak and almost
555 insignificant during post-CP El Niño late summers (Figs. 18N, 18O, 18Q and 18R).
556 Similar conclusions could be drawn from the other two classification methods
557 (Supplementary Figs. 17 and 19) and extended time periods (Supplementary Figs. 16,
558 18 and 20). To get insight into the mechanisms of AAC patterns during post-EP and
559 post-CP El Niño summers, the composite SSTA patterns are further shown
560 (Supplementary Figs. 21, 22 and 23). The simulated NIO–WP SSTA gradients during
561 post-EP El Niño summers are generally consistent with those during the entire post-El
562 Niño summers in CMIP models. However, the WP warming bias is too westward-
563 extended in CMIP models during post-CP El Niño summers. As a result, the simulated
564 NIO–WP SSTA gradients could barely persist, which may lead to the disappearance of

AAC during post-CP El Niño late summer.

The weak persistence bias of summertime AAC will inevitably lead to an overall underestimation of summer seasonal mean AAC. Thus, future studies should be careful when evaluating and projecting El Niño-related summer AAC and coherent climate impacts in CMIP5 and CMIP6 models. We recommend that models with relatively high simulation skills should be selected first rather than simply using all available model simulations. Here, we use the monthly AAC index to preliminarily identify the most skillful CMIP models. Future studies could use more comprehensive metrics to select high-skill models based on their particular applications or societal needs. In this section, if the AAC indices of a single model in June(1), July(1) and August(1) surpass 1 simultaneously, it will be deemed as the high-performance model. Slight varying thresholds (0.8 and 1.2) will not change the composite results. Three CMIP5 models (CESM1-WACCM, GFDL-CM3, NorESM1-ME) and eight CMIP6 models (CESM2-FV2, CESM2-WACCM-FV2, CESM2, E3SM-1-1-ECA, E3SM-1-1, GISS-E2-1-H, KACE-1-0-G, MIROC-ES2L) are selected based on this criterion. The selected optimal model set MME performs significantly better than the whole CMIP5/6 ensemble. The general characteristics of the observed AAC and precipitation anomalies in August(1) can be well captured (Figs. 19H and 19I). Correspondingly, the IOB warming strongly maintains while WP warming bias dissipates during post-El Niño late summer in the high-performance CMIP5 and CMIP6 MME (Figs. 20H and 20I). In addition, we observe a more realistic simulation of mean-state SWIO thermocline dome and equatorial Pacific cold tongue in the high-performance CMIP5 and CMIP6 MME than their raw counterparts (Supplementary Figs. 24 and 25). This mean-state simulation improvement may contribute to the generally good persistence of the NIO–WP SSTA gradient in high-performance models (Fig. 20).

6. Summary

591 The present study provides a systematical investigation of weak persistence of AAC
592 during post-El Niño summers and unveils its possible physical mechanisms based on
593 45 CMIP6 and 36 CMIP5 models. In contrast with the observational sub-seasonal
594 intensification, the simulated AAC fails to persist through post-El Niño summers in the
595 CMIP5 and CMIP6 MME. Here, we suggest that the weak persistence of NIO–WP
596 SSTA gradient rooted in the poorly represented climate background mean-states may
597 be responsible for biased persistence of AAC during post-El Niño summers (Fig. 21).
598 On one hand, the IOB warming decays faster in CMIP5 and CMIP6 MME compared
599 with the observations during post-El Niño summers. Upper-ocean heat budget
600 diagnoses indicate that the weak persistence of anomalous latent heat flux and
601 shortwave radiation should be largely responsible for that of the IOB warming. The
602 simulated thermocline dome in SWIO is much deeper in CMIP5 and CMIP6 MME
603 compared with the observation. It may lead to weaker oceanic Rossby wave-induced
604 thermocline feedback and weakened cross-equatorial C-shaped wind patterns during
605 post-El Niño spring and early summer. The weakened northeasterly wind anomalies
606 over NIO cause the dampened WES feedback and reduced latent heating anomalies,
607 finally resulting in the weak persistence of IOB warming. The weak persistence of inter-
608 basin positive feedback between IOB warming and AAC pattern also plays a major role.
609 On the other hand, the WP warming bias persists throughout post-El Niño summer in
610 CMIP5 and CMIP6 MME and ocean dynamic processes play an important role in this
611 case. Specifically, the simulated mean-state cold tongue in the WP is colder and more
612 westward-extended in CMIP5 and CMIP6 MME than in the observation, resulting in
613 the intensified upper-ocean zonal advection feedback and wind–downwelling–SST
614 feedback, thereby favoring the persistence of WP warming bias throughout post-El
615 Niño summers. This long-lasting unrealistic WP warming bias may excite westward
616 spreading Rossby wave and attenuate NIO warming-induced eastward propagating
617 Kelvin wave, finally leading to the weak persistence of AAC. Apart from the NIO–WP

SSTA gradient, the weakened background NWP summer monsoon onset in CMIP models may suppress increase of moist/convection–circulation feedback intensity in August(1), which may result in the weakened summertime AAC intensification compared with the observation.

Previous studies suggested that SWIO deep thermocline bias may stem from IO Dipole-like bias (Li et al. 2015; Zheng et al. 2016) while the equatorial cold tongue bias may originate from the misrepresented ocean–atmosphere feedback in the Pacific in CMIP models (Li and Xie 2014). Compared with CMIP5 models, CMIP6 models simulate a more realistic SWIO thermocline dome and equatorial Pacific cold tongue, though evidence for the latter is less robust. As a result, CMIP6 models could simulate a more realistic AAC persistence than their CMIP5 counterparts. The weak persistence bias of summer AAC may potentially restrict the models' prediction and projection skills in the Asian monsoon during late summer. Therefore, the present study highlights the significance of a more realistic simulation of mean-state SWIO thermocline dome and equatorial Pacific cold tongue to better reproduce the persistence of summer AAC and its climate impacts in CGCMs.

It is noteworthy that the AAC could result in positive SSTA in the NWP and south China sea (Figs. 4A, 4D and 4G), which will strengthen the local deep convection and decrease the downward shortwave radiation, thereby damping the AAC and forming the negative cloud–radiation–SST feedback. Thus, local positive SSTA and WP warming bias tend to dissipate the AAC pattern, whereas the NIO warming maintains the AAC during post-El Niño summers. In August(1), the damping effects outweigh the IO capacitor effect in CMIP models, leading to the rapid decay of AAC over the EA–NWP. In addition to SSTA pattern impacts, the anomalous subtropical Meiyu/Baiu rainfall serving as the heat source may also be vital in anchoring the AAC pattern (Lu and Lin 2009). In the observational August(1), the AAC induces and is in turn

644 geographically fixed by the anomalous rainband in its northern flank (Fig. 1G).
645 However, the AAC displaces eastward and disappears over EA in August(1) in CMIP5
646 and CMIP6 MME (Figs. 1H and 1I), resulting in the vanishment of anomalous rainband.
647 Without the positive feedback from this subtropical rainfall-induced heating anomaly,
648 the AAC is more loosely organized and far away from the mainland in CMIP models.
649 Previous researches have suggested that NIO SSTA depend largely on the simulated
650 ENSO in the Pacific via the atmospheric bridge (Klein et al. 1999; Alexander et al.
651 2002). Whether the weak persistence of IOB warming interacts with long-lasting WP
652 warming bias is intriguing and entails future study.
653

Acknowledgements

We would like to thank two anonymous reviewers for their insightful and constructive comments that significantly improve the quality of the manuscript. We also acknowledge the World Climate Research Programme's Working Group on Coupled Modelling, and we thank the climate modeling groups across the world (listed in Table 1) for producing and making publicly available their model outputs.

Funding

This work is supported by the National Basic Research Program of China (2019YFA0606703), the Strategic Priority Research Program of Chinese Academy of Sciences (XDA20060500), the National Natural Science Foundation of China (42175040,41831175,41661144016), Key Deployment Project of Centre for Ocean Mega-Research of Science, Chinese Academy of Sciences (COMS2019Q03). The work was also supported by the Chinese Jiangsu Collaborative Innovation Center for Climate Change and the Youth Innovation Promotion Association of CAS (2021072).

Data Availability Statement

All the data that support the findings are available for open access. The CMAP precipitation data is located at https://psl.noaa.gov/data/gridded/data.cmap.html. The CMIP5/6 model outputs can be accessed at the ESGF portal (https://esgf-node.llnl.gov/projects/esgf-llnl/). The NCEP–NCAR atmospheric reanalysis is located at https://psl.noaa.gov/data/gridded/data.ncep.reanalysis.html. HadISST dataset could be accessed from https://www.metoffice.gov.uk/hadobs/hadisst/. SODA datasets could be accessed from http://www2.atmos.umd.edu/~ocean/index_files/. All the codes for analyses and diagnostics are available from the corresponding authors upon reasonable request.

Author Contributions

679 HT, KH, and GH conceived the study, designed the methodology and built the
680 mechanisms. HT performed the formal analyses and wrote the draft manuscript. GH,
681 KH, WJ, WT, YW and HH contributed to improving the manuscript and assisted in the
682 interpretation of the results.

683 **Competing interests**

684 The authors have no competing interests as defined by Springer, or other interests
685 that might be perceived to influence the results and/or discussion reported in this paper.

686

687 **References**

688 Alexander MA, Blade I, Newman M, Lanzante JR, Lau N-C, Scott JD (2002) The
689 atmospheric bridge: The influence of ENSO teleconnections on air–sea interaction
690 over the global oceans. J Clim 15:2205–2231

691 Ashok K, Behera SK, Rao SA, Weng H, Yamagata T (2007) El Niño Modoki and its
692 possible teleconnection. J Geophys Res Oceans 112:1–27

693 Carton JA, Giese BS (2008) A reanalysis of ocean climate using simple ocean data
694 assimilation (SODA). Mon Weather Rev 136:2999–3017

695 Chang CP, Zhang Y, Li T (2000) Interannual and Interdecadal Variations of the East
696 Asian Summer Monsoon and Tropical Pacific SSTs. Part I: Roles of the
697 Subtropical Ridge. J Clim 13(24):4310–4325

698 Chen M, Li T, Shen X, Wu B (2016) Relative roles of dynamic and thermodynamic
699 processes in causing evolution asymmetry between El Niño and La Niña. J Clim
700 29:2201–2220

701 Chen M, Li T (2021) ENSO evolution asymmetry: EP versus CP El Niño. Clim Dyn
702 56(11):3569–3579

703 Chowdary JS, Xie S-P, Lee J-Y, Kosaka Y, Wang B (2010) Predictability of summer
704 northwest Pacific climate in 11 coupled model hindcasts: local and remote forcing.
705 J Geophys Res Atmos 115:1–16

706 Chowdary JS, Gnanaseelan C, Chakravorty S (2013) Impact of Northwest Pacific
707 anticyclone on the Indian summer monsoon region. Theor Appl Climatol 113:329–
708 336

709 Deng K, Yang S, Ting M, Zhao P, Wang Z (2019) Dominant modes of China summer
710 heat waves driven by global sea surface temperature and atmospheric internal

711 variability. J Clim 32:3761–3775

712 Du Y, Xie SP, Huang G, Hu K (2009) Role of air–sea interaction in the long persistence
713 of El Niño-induced north Indian Ocean warming. J Clim 22(8):2023–2038

714 Du Y, Yang L, Xie SP (2011) Tropical Indian Ocean Influence on Northwest Pacific
715 Tropical Cyclones in Summer Following Strong El Nino. J Clim 24 (1):315–322

716 Du Y, Xie S-P, Yang Y-L, Zheng X-T, Liu L, Huang G (2013) Indian Ocean variability
717 in the CMIP5 multimodel ensemble: the basin mode. J Clim 26(18):7240–7266

718 Du Y, Chen Z, Xie S-P, Zhang L, Zhang Y, Cai Y (2022) Drivers and characteristics of
719 the Indo-western Pacific Ocean capacitor. Front Clim 4:1014138

720 Eyring V, Bony S, Meehl GA, Senior CA, Stevens B, Stoufer RJ, Taylor KE (2016)
721 Overview of the Coupled Model Intercomparison Project Phase 6 (CMIP6)
722 experimental design and organization. Geosci Model Dev 9(5):1937–1958

723 Feng J, Chen W, Tam CY, Zhou W (2011) Different impacts of El Niño and El Niño
724 Modoki on China rainfall in the decaying phases. Int J Climatol 31:2091–2101

725 Freund MB, Brown JR, Henley BJ, Karoly DJ, Brown JN (2020) Warming patterns
726 affect El Niño diversity in CMIP5 and CMIP6 models. J Clim 33(19):8237–8260

727 Gill AE (1980) Some simple solutions for heat-induced tropical circulation. Q J R
728 Meteorol Soc 106:447–462

729 Grose MR, Narsey S, Delage FP et al (2020) Insights from CMIP6 for Australia's future
730 climate. Earth's Future 8:e2019EF001469

731 He C, Zhou T (2015) Responses of the Western North Pacific subtropical high to global
732 warming under RCP4.5 and RCP8.5 scenarios projected by 33 CMIP5 models: the
733 dominance of tropical Indian Ocean–tropical Western Pacific SST gradient. J Clim
734 28:365–380

735 Hou M, Tang Y (2022) Recent progress in simulating two types of ENSO–from CMIP5
736 to CMIP6. Front Mar Sci 9:986780

737 Hu K, Huang G, Huang R (2011) The impact of tropical Indian Ocean variability on
738 summer surface air temperature in China. J Clim 24(20):5365–5377

739 Hu K, Huang G, Zheng X-T, Xie S-P, Qu X, Du Y, Liu L (2014) Interdecadal variations
740 in ENSO influences on Northwest Pacific-East Asian early summertime climate
741 simulated in CMIP5 models. J Clim 27(15):5982–5998

742 Hu K, Huang G, Xie S-P, Long S-M (2019) Effect of the mean flow on the anomalous
743 anticyclone over the Indo-Northwest Pacific in post-El Niño summers. Clim Dyn
744 53(9–10):5725–5741

745 Hu K, Huang G, Huang P, Kosaka Y, Xie S-P (2021) Intensification of El Nino-induced
746 atmospheric anomalies under greenhouse warming. Nat Geosci 14:377–382

747 Huang RH, Sun FY (1992) Impacts of the tropical western pacific on the East-Asian
748 summer monsoon. J Meteorol Soc Jpn 70(1B):243–256

749 Jiang W, Huang G, Hu K, Wu R, Gong H, Chen XL, Tao W (2017) Diverse relationship
750 between ENSO and the northwest Pacific summer climate among CMIP5 models:
751 dependence on the ENSO decay pace. J Clim 30:109–127

752 Jiang W, Huang G, Huang P, Wu R, Hu K, Chen W (2019) Northwest Pacific
753 anticyclonic anomalies during Post-El Niño summers determined by the pace of
754 El Niño Decay. J Clim 32:3487–3503

755 Jiang W, Huang P, Huang G, Ying J (2021) Origins of the excessive westward extension
756 of ENSO SST simulated in CMIP5 and CMIP6 models. J Clim 34(8):2839–2851

757 Jiang W, Gong H, Huang P, Wang L, Huang G, Hu L (2022) Biases and improvements
758 of the ENSO-East Asian winter monsoon teleconnection in CMIP5 and CMIP6

759 models. Clim Dyn 59:2467–2480

760 Jiang Z, Li J (2022) Impact of eastern and central Pacific El Niño on lower tropospheric
761 ozone in China. Atmos Chem Phys 22(11):7273–7285

762 Kalnay E, Kanamitsu M, Kistler R, Collins W, Deaven D, Gandin L, Iredell M, Saha S,
763 White G, Woollen J, Zhu Y, Chelliah M, Ebisuzaki W, Higgins W, Janowiak J, Mo
764 KC, Ropelewski C, Wang J, Leetmaa A, Reynolds R, Jenne R, Joseph D (1996)
765 The NCEP/NCAR 40-year reanalysis project. Bull Am Meteorol Soc 77(3):437–
766 471

767 Kim H-M, Webster PJ, Curry JA, Toma VE (2012) Asian summer monsoon prediction
768 in ECMWF System 4 and NCEP CFSv2 retrospective seasonal forecasts. Clim
769 Dyn 39:2975–2991

770 Klein SA, Soden BJ, Lau N-C (1999) Remote sea surface temperature variations during
771 ENSO: Evidence for a tropical atmospheric bridge. J Clim 12:917–932

772 Kosaka Y, Xie S-P, Lau NC, Vecchi GA (2013) Origin of seasonal predictability for
773 summer climate over the Northwestern Pacific. Proc Natl Acad Sci 110(19):7574–
774 7579

775 Kug JS, Choi J, An SI, Jin FF, Wittenberg AT (2010) Warm pool and cold tongue El
776 Niño events as simulated by the GFDL 2.1 coupled GCM. J Clim 23(5):1226–
777 1239

778 Lee T, Waliser DE, Li J-L, Landerer FW, Gierach MM (2013) Evaluation of CMIP3
779 and CMIP5 wind stress climatology using satellite measurements and atmospheric
780 reanalysis products. J Clim 26(16):5810–5826

781 Li G, Xie S-P (2014) Tropical biases in CMIP5 multimodel ensemble: the excessive
782 equatorial Pacific cold tongue and double ITCZ problems. J Clim 27:1765–1980

783 Li G, Xie S-P, Du Y (2015) Climate model errors over the South Indian Ocean
784 thermocline dome and their effect on the basin mode of interannual variability. J
785 Clim 28:3093–8

786 Li G, Jian Y, Yang S, Du Y, Wang Z, Li Z, Zhuang W, Jiang W, Huang G (2019) Effect
787 of excessive equatorial Pacific cold tongue bias on the El Niño-Northwest Pacific
788 summer monsoon relationship in CMIP5 multi-model ensemble. Clim Dyn 52(9–
789 10):6195–6212

790 Li S, Gong Z, Zhang S, Yang J, Qiao S, Feng G (2022) Decadal variation of the
791 precipitation relationship between June and August over South China and its
792 mechanism. Clim Dyn 59:1863–1882

793 Li T, Wang B, Wu B, Zhou TJ, Chang CP, Zhang RH (2017) Theories on formation of
794 an anomalous anticyclone in western North Pacific during El Niño: a review. J
795 Meteorol Res 31:987–1006

796 Lu R, Lin Z (2009) Role of subtropical precipitation anomalies in maintaining the
797 summertime meridional teleconnection over the Western North Pacific and East
798 Asia. J Clim 22:2058–2072

799 Matsuno T (1966) Quasi-geostrophic motions in the equatorial area. J Meteorol Soc Jpn
800 44:25–43

801 McPhaden MJ, Zebiak SE, Glantz MH (2006) ENSO as an integrating concept in Earth
802 science. Science 314:1740–1745

803 Nitta T (1987) Convective activities in the tropical western Pacific and their impact on
804 the northern hemisphere summer circulation. J Meteorol Soc Jpn 65:165–171

805 Ohba M, Ueda H (2006) A role of zonal gradient of SST between the Indian Ocean and
806 the Western Pacific in localized convection around the Philippines. SOLA 2:176–

179

Planton YY, Guilyardi E, Wittenberg AT, Lee J, Gleckler PJ, Bayr T, McGregor S, McPhaden MJ, Power S, Roehrig R, Vialard J, Voldoire A (2021) Evaluating climate models with the CLIVAR 2020 ENSO metrics package. Bull Am Meteorol Soc 102(2):E193–E217

Rayner NA, Parker DE, Horton EB, Folland CK, Alexander LV, Rowell DP, Kent EC, Kaplan A (2003) Global analyses of sea surface temperature, sea ice, and night marine air temperature since the late nineteenth century. J Geophys Res Atmos 108(D14):4407

Ren HL, Jin FF (2011) Niño indices for two types of ENSO. Geophys Res Lett 38:L04704

Takaya K, Nakamura H (2001) A Formulation of a Phase-Independent Wave-Activity Flux for Stationary and Migratory Quasi-geostrophic Eddies on a Zonally Varying Basic Flow. J Atmos Sci 58(6):608–627

Tang H, Wang Z, Tang B, Ma Y, Pei L, Tian F, Wang J, Nanding N, Sparrow S, Tett S, Dong B, Lott F (2022a) Reduced probability of 2020 June–July persistent heavy Meiyu rainfall event in the mid-lower reaches of the Yangtze River basin under anthropogenic forcing. Bulletin America Meteorology Social 103(3):S83–S89

Tang HS, Wang J, Hu KM, Huang G, Chowdary JS, Wang Y, Wang Z, Tang B (2022b) Increasing 2020-like boreal summer rainfall extremes over Northeast Indian subcontinent under greenhouse warming. Geophys Res Lett 49(11):e2021GL096377

Tang HS, Hu KM, Huang G, Wang Y, Tao W (2021) Intensification and Northward extension of Northwest Pacific anomalous anticyclone in El Niño decaying mid-summer: an energetic perspective. Clim Dyn 58:591–606

832 Tao SY, Chen LX (1987) A review of recent research on the East Asian summer
833 monsoon in China. Monsoon meteorology (Chang CP, Krishnamurti TN (eds)).
834 Oxford University Press, New York

835 Tao W, Huang G, Hu K, Gong H, Wen G, Liu L (2016) A study of biases in simulation
836 of the Indian Ocean basin mode and its capacitor effect in CMIP3/CMIP5 models.
837 Clim Dyn 46:205–226

838 Tao W, Huang G, Wu R, Hu K, Wang P, Gong H (2018) Origins of biases in CMIP5
839 Models simulating Northwest Pacific summertime atmospheric circulation
840 anomalies during the decaying phase of ENSO. J Clim 31(14):5707–5729

841 Tao W, Wang P, Liu Y, Wen G, Dong D (2019) Dominant modes of CMIP3/5 models
842 simulating northwest Pacific circulation anomalies during post-ENSO summer
843 and their SST dependence. Theor Appl Climatol 138:1809–1820

844 Taylor KE, Stouffer RJ, Meehl GA (2012) An overview of CMIP5 and the experiment
845 design. Bull Am Meteorol Soc 93(4):485–498

846 Wang B, Fan Z (1999) Choice of South Asian summer monsoon indices. Bull Amer
847 Meteor Soc, 80:629–638

848 Wang B, Wu R, Fu X (2000) Pacific-East Asian Teleconnection: How Does ENSO
849 Affect East Asian Climate? J Clim 13(9):1517–1536

850 Wang X, Li T, He C (2021) Impact of the mean state on El Niño induced western North
851 Pacific anomalous anticyclone during its decaying summer in AMIP models. J
852 Clim 34(22):1–49

853 Wu B, Zhou TJ, Li T (2009) Seasonally evolving dominant interannual variability
854 modes of East Asian climate. J Clim 22(11):2992–3005

855 Wu B, Li T, Zhou TJ (2010) Relative contributions of the Indian Ocean and local SST

856 anomalies to the maintenance of the western North Pacific anomalous anticyclone
857 during the El Niño decaying summer. J Clim 23(11):2974–2986

858 Wu RG, Kirtman BP, Krishnamurthy V (2008) An asymmetric mode of tropical Indian
859 Ocean rainfall variability in boreal spring. J Geophys Res Atmos 113:D05104

860 Xiang B, Wang B, Yu W, Xu S (2013) How can anomalous western North Pacific
861 Subtropical High intensify in late summer? Geophys Res Lett 40(10):2349–2354

862 Xie P, Arkin PA (1997) Global precipitation: A 17-year monthly analysis based on
863 gauge observations, satellite estimates. Bull Am Meteorol Soc 78(11):2539–2558

864 Xie SP, Annamalai H, Schott F, McCreary JP (2002) Structure and mechanisms of south
865 Indian Ocean climate variability. J Clim 15:864–878

866 Xie S-P, Hu K, Hafner J, Tokinaga H, Du Y, Huang G, Sampe T (2009) Indian Ocean
867 Capacitor Effect on Indo–Western Pacific Climate during the Summer following
868 El Niño. J Clim 22(3):730–747

869 Xie S-P, Deser C, Vecchi GA, Ma J, Teng H, Wittenberg AT (2010) Global warming
870 pattern formation: sea surface temperature and rainfall. J Clim 23(4):966–986

871 Xie S-P, Kosaka Y, Du Y, Hu K, Chowdary JS, Huang G (2016) Indo-western Pacific
872 Ocean capacitor and coherent climate anomalies in post-ENSO summer: A review.
873 Adv Atmos Sci 33(4):411–432

874 Xu K, Tam CY, Zhu C, Liu B, Wang W (2017) CMIP5 projections of two types of El
875 Niño and their related tropical precipitation in the twenty-first century. J
876 Clim 30(3):849–864

877 Yang X, Huang P (2022) Improvements in the relationship between tropical
878 precipitation and sea surface temperature from CMIP5 to CMIP6. Climate Dyn
879 https://doi.org/10.1007/s00382-022-06519-3

Ye H, Lu R (2010) Subseasonal Variation in ENSO-Related East Asian Rainfall Anomalies during Summer and Its Role in Weakening the Relationship between the ENSO and Summer Rainfall in Eastern China since the Late 1970s. J Clim 24(9):2271–2284

Yeh SW, Kug JS, Dewitte B, Kwon MH, Kirtman BP, Jin FF (2009) El Niño in a changing climate. Nature 461:511–514

Yu JY, Zou Y, Kim ST, Lee T (2012) The changing impact of El Niño on US winter temperatures. Geophys Res Lett 39(15):L15702

Yu JY, Kim ST (2013) Identifying the types of major El Niño events since 1870. Int J Climatol 33(8):2105-2112

Yu T, Feng J, Chen W, Wang X (2021) Persistence and breakdown of the western North Pacific anomalous anticyclone during the EP and CP El Niño decaying spring. Climate Dyn 57:3529–3544

Yuan Y, Yang S (2012) Impacts of different types of El Niño on the East Asian climate: Focus on ENSO cycles. J Clim 25:7702–7722

Zheng X-T, Gao L, Li G, Du Y (2016) The southwest Indian Ocean thermocline dome in CMIP5 models: historical simulation and future projection. Adv Atmos Sci 33:489–503

Zou Y, Yu JY, Lee T, Lu MM, Kim ST (2014) CMIP5 model simulations of the impacts of the two types of El Niño on the US winter temperature. J Geophys Res Atmos 119(6):3076–3092

Table 1. Details of 45 CMIP6 and 36 CMIP5 models used in the present study. The high-skill models are highlighted by an asterisk.

CMIP6 (45)	Atmos. Resolution (lat × lon)	CMIP5 (36)	Atmos. Resolution (lat × lon)	Institute
ACCESS-CM2	1.25°×1.875°	ACCESS1-0	1.24°×1.875°	CSIRO–BOM/Australia
ACCESS-ESM1-5	1.24°×1.875°	ACCESS1-3	1.24°×1.875°	
BCC-CSM2-MR	1.125°×1.125°	bcc-csm1-1-m	1.125°×1.125°	BCC-CMA/China
BCC-ESM1	2.81°×2.81°	bcc-csm1-1	2.81°×2.81°	
/	/	BNU-ESM	2.81°×2.81°	BNU/China
CAMS-CSM1-0	1.125°×1.125°	/	/	CAMS/China
CanESM5-CanOE	2.81°×2.81°	/	/	CCCma/Canada
CanESM5	2.81°×2.81°	CanESM2	2.81°×2.81°	
CESM2-FV2*	1.875°×2.5°	CESM1-BGC	0.94°×1.25°	NSF-DOE-NCAR/United States
CESM2-WACCM-FV2*	1.875°×2.5°	CESM1-CAM5	0.94°×1.25°	
CESM2-WACCM	0.94°×1.25°	CESM1-WACCM*	1.875°×2.5°	
CESM2*	0.94°×1.25°	CCSM4	0.94°×1.25°	
/	/	CESM1-FASTCHEM	0.94°×1.25°	
/	/	CMCC-CESM	3.75°×3.75°	CMCC/Italy
/	/	CMCC-CMS	1.875°×1.875°	
/	/	CMCC-CM	0.75°×0.75°	
CNRM-CM6-1-HR	0.5°×0.5°	/	/	CNRM-CERFACS/France
CNRM-CM6-1	1.4°×1.4°	CNRM-CM5	1.4°×1.4°	
CNRM-ESM2-1	1.4°×1.4°	/	/	
/	/	CSIRO-Mk3-6-0	1.875°×1.875°	CSIRO/Australia
E3SM-1-0	1°×1°	/	/	E3SM-Project/United States
E3SM-1-1-ECA*	1°×1°	/	/	
E3SM-1-1*	1°×1°	/	/	
EC-Earth3-Veg	0.7°×0.7°	/	/	

EC-Earth3	0.7°×0.7°	/	/	
FGOALS-f3-L	1°×1.25°	FGOALS-s2	1.67°×2.81°	LASG-CESS/China
FGOALS-g3	2.25°×2°	FGOALS-g2	3°×2.81°	
/	/	FIO-ESM	2.81°×2.81°	FIO/China
GFDL-CM4	1°×1.25°	GFDL-CM3*	2°×2.5°	NOAA-GFDL/United States
GFDL-ESM4	1°×1.25°	GFDL-ESM2G	2°×2.5°	
/	/	GFDL-ESM2M	2°×2.5°	
GISS-E2-1-G-CC	2°×2.5°	/	/	NASA-GISS/United States
GISS-E2-1-G	2°×2.5°	GISS-E2-R	2°×2.5°	
GISS-E2-1-H*	2°×2.5°	GISS-E2-H	2°×2.5°	
HadGEM3-GC31-LL	1.25°×1.875°	/	/	MOHC/United Kingdom
HadGEM3-GC31-MM	0.56°×0.83°	/	/	
INM-CM4-8	1.5°×2°	inmcm4	1.5°×2°	INM/Russia
INM-CM5-0	1.5°×2°	/	/	
IPSL-CM6A-LR	1.26°×2.5°	IPSL-CM5A-LR	1.875°×3.75°	IPSL/France
/	/	IPSL-CM5A-MR	1.26°×2.5°	
/	/	IPSL-CM5B-LR	1.875°×3.75°	
KACE-1-0-G*	1.25°×1.875°	/	/	NIMS-KMA/Korea
MCM-UA-1-0	2.25°×3.75°	/	/	UA/United States
MIROC-ES2L*	2.81°×2.81°	MIROC-ESM	2.81°×2.81°	MIROC/Japan
/	/	MIROC-ESM-CHEM	2.81°×2.81°	
MIROC6	1.4°×1.4°	MIROC5	1.4°×1.4°	
MPI-ESM-1-2-HAM	1.875°×1.875°	/	/	DKRZ/German
MPI-ESM1-2-HR	0.94°×0.94°	MPI-ESM-MR	1.875°×1.875°	
MPI-ESM1-2-LR	1.875°×1.875°	MPI-ESM-LR	1.875°×1.875°	
MRI-ESM2-0	1.125°×1.125°	MRI-CGCM3	1.125°×1.125°	MRI/Japan
NESM3	1.875°×1.875°	/	/	NUIST/China
NorCPM1	1.875°×2.5°	NorESM1-M	1.875°×2.5°	NCC-NMI/Norway

NorESM2-LM	1.875°×2.5°	NorESM1-ME*	1.875°×2.5°	
NorESM2-MM	0.94°×1.25°	/	/	
SAM0-UNICON	0.94°×1.25°	/	/	SUU/Korea
UKESM1-0-LL	1.25°×1.875°	/	/	MOHC/United Kingdom

903

904

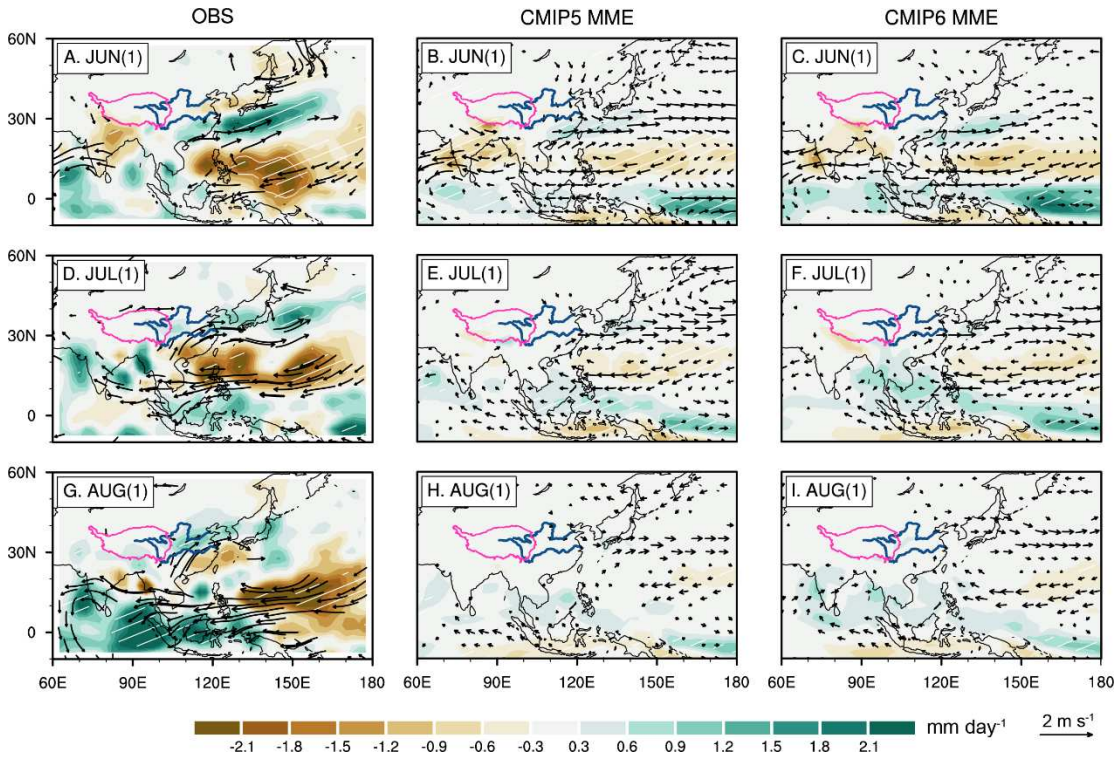

905

906 **Figure 1.** 850-hPa wind (vectors; units: $m\ s^{-1}$) and precipitation (colors; units: $mm\ day^{-1}$) anomalies for
907 the El Niño composite in the observations (left panels), CMIP5 MME (middle panels), and CMIP6 MME
908 (right panels) in June(1) (A, B, C), July(1) (D, E, F), and August(1) (G, H, I). The Tibetan Plateau is
909 highlighted in pink curve and has been masked out before plotting. The Yangtze River and the Yellow River
910 are highlighted in blue curves. Vectors only exceeding the 95% confidence level are shown. White hatchings
911 denote that the anomalies are significant at the 95% confidence level (for observations) or more than 80% of
912 models agree with the sign of the MME (for CMIP models).

913

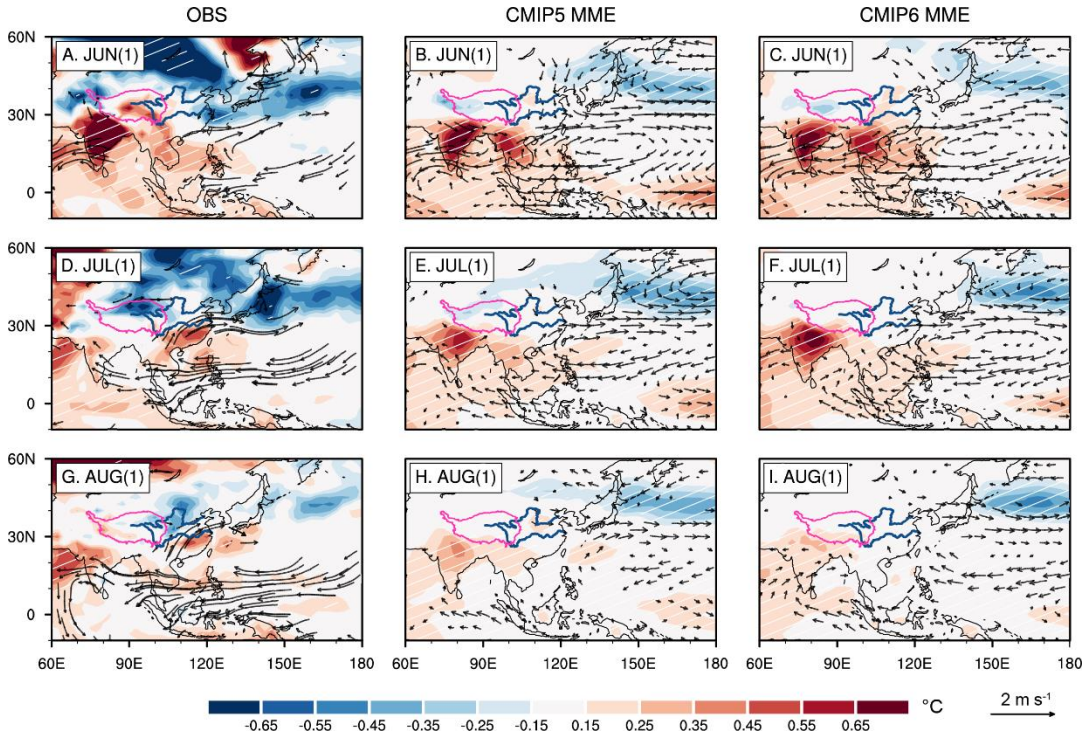

Figure 2. Same as Fig. 1, but colors for SAT anomalies (units: ℃).

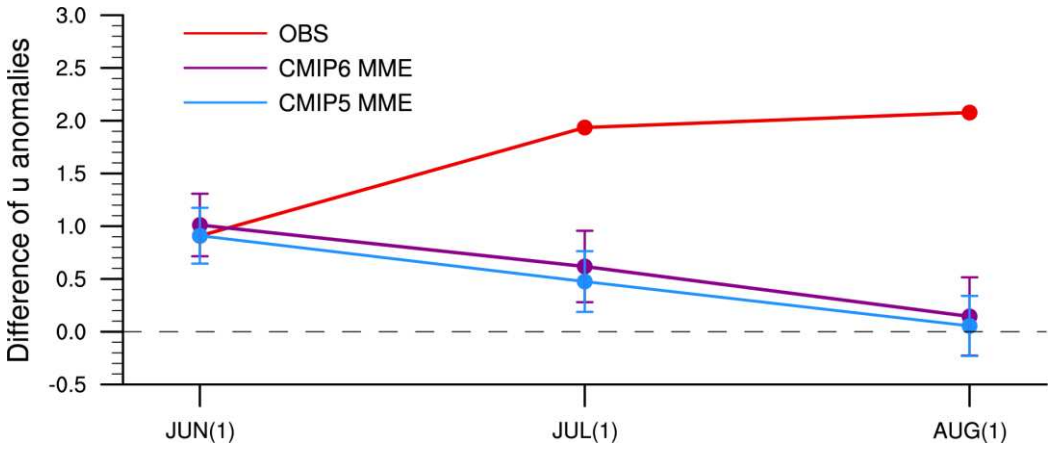

Figure 3. Temporal evolutions of the AAC index, i.e., difference of 850-hPa zonal winds between a northern region (20°–30°N, 110°–140°E) and a southern region (5°–15°N, 100°–130°E), for the El Niño composite in observations (red line), CMIP5 MME (light blue line), and CMIP6 MME (purple line). Error bars for the CMIP5 and CMIP6 MME denote ± 1-fold standard deviation of inter-model variability among 45 CMIP6 and 36 CMIP5 models, respectively.

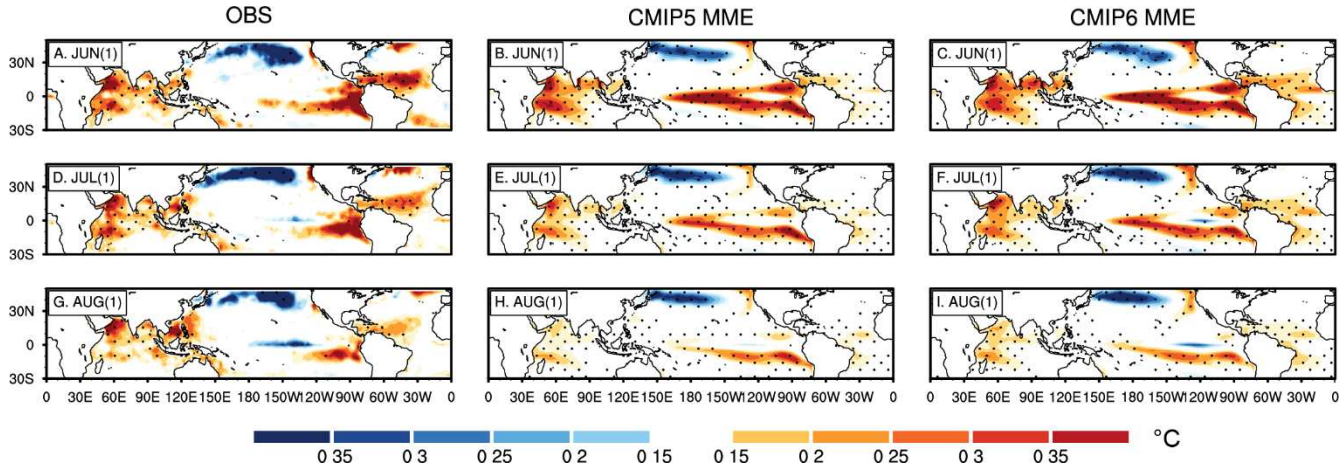

924

925 **Figure 4.** SSTA (colors; units: ℃) for the El Niño composite in the observations (left panels), CMIP5 MME
926 (middle panels), and CMIP6 MME (right panels) in June(1) (A, B, C), July(1) (D, E, F), and August(1) (G, H,
927 I). Stippling denotes that the anomalies are significant at the 95% confidence level (for observation) or more
928 than 80% of models agree with the sign of the MME (for CMIP models).

929

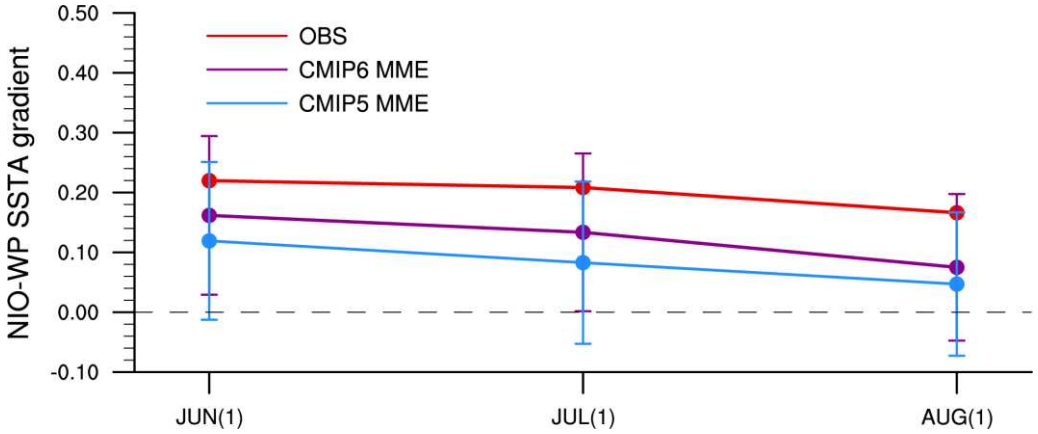

930

931 **Figure 5.** Same as Fig. 3, but for SSTA gradient between NIO and WP (units: ℃) from June(1) to August(1).

932

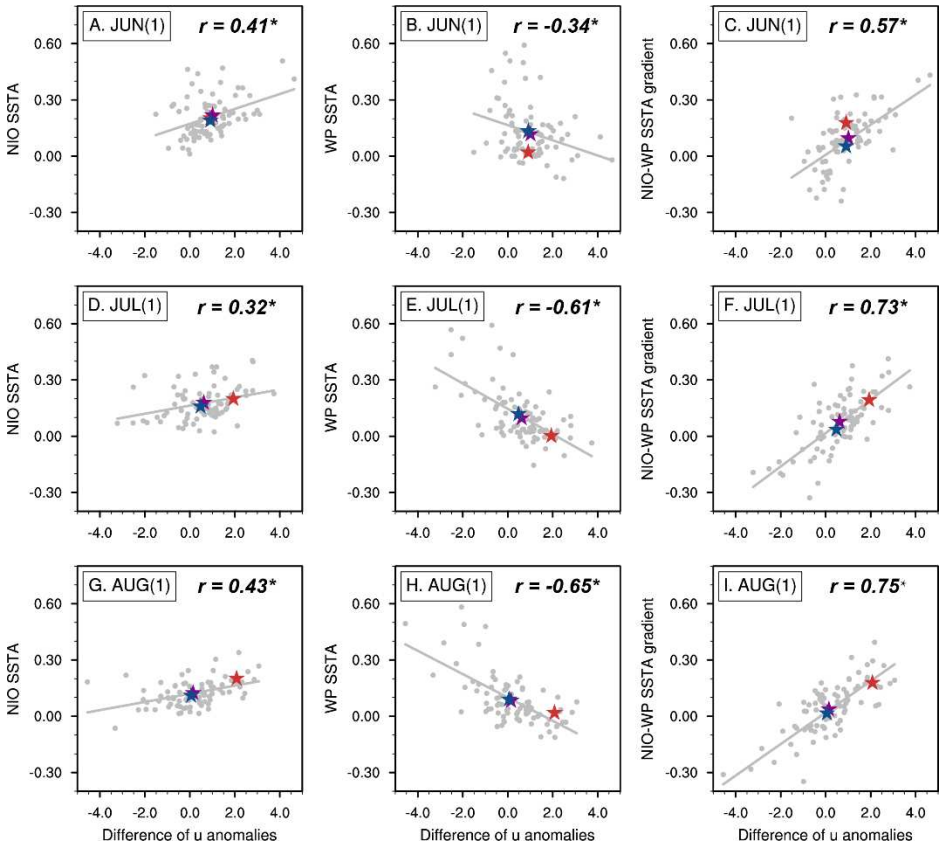

933

934 **Figure 6.** Scatterplot between AAC index and SSTA averaged over the NIO (0°–20°N, 50°–120°E; left panels),
935 WP (10°S–10°N, 140°E–170°W; middle panels), and NIO–WP SSTA gradient (right panels) for the El Niño
936 composite in June(1) (A, B, C), July(1) (D, E, F), and August(1) (G, H, I). The grey solid circles denote CMIP
937 models, while the red, blue and purple stars represent the observations, CMIP5 MME and CMIP6 MME,
938 respectively. The linear regression lines are also shown in each subgraph. The asterisk denotes the regression
939 is statistically significant at $p < 0.01$ level based on the Student's t-test.

940

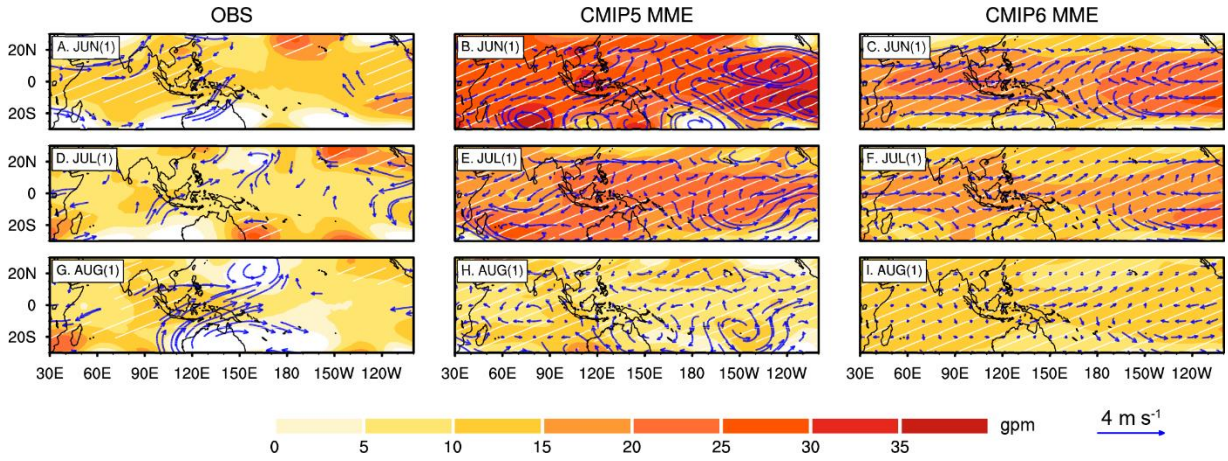

941

942 **Figure 7.** Same as Fig. 1, but colors for 200-hPa geopotential height anomalies (units: gpm) and vectors for

943 200-hPa wind anomalies (units: $m\ s^{-1}$).

944

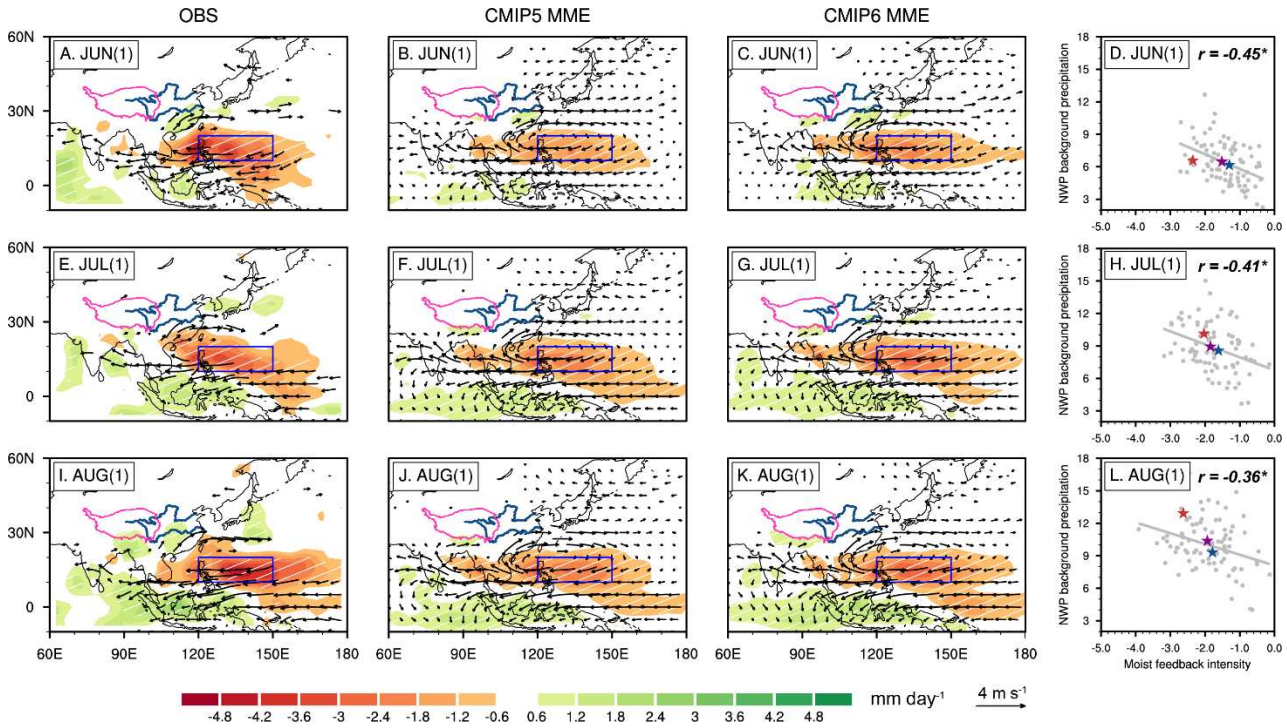

945

946 **Figure 8.** 850-hPa wind (vectors; units: $m\,s^{-1}$) and precipitation (colors; units: $mm\,day^{-1}$) anomalies
947 regressed onto the standardized AAC index in observations (left panels), CMIP5 MME (middle panels), and
948 CMIP6 MME (right panels) in June(1) (A, B, C), July(1) (E, F, G), and August(1) (I, J, K). The Tibetan Plateau
949 is highlighted in pink curve and has been masked out before plotting. The Yangtze River and the Yellow River
950 are highlighted in blue curves, while the key region of moist feedback (10°–20°N, 120°–150°E) is highlighted
951 in blue box. Vectors only exceeding the 95% confidence level are shown. White hatchings denote that the
952 anomalies are significant at the 95% confidence level (for observations) or more than 80% of models agree
953 with the sign of the MME (for CMIP models). Scatterplots between moist feedback intensity (units:
954 $mm\,day^{-1}$) and NWP background precipitation (units: $mm\,day^{-1}$) in June(1) (D), July(1) (H), and
955 August(1) (L) are shown as well. Larger negative value indicates the stronger moist feedback. The grey solid
956 circles denote CMIP models, while the red, blue and purple stars represent the observations, CMIP5 MME
957 and CMIP6 MME, respectively. The linear regression lines are also shown in each scatterplot. The asterisk
958 denotes the regression is statistically significant at $p < 0.01$ level based on the Student's t-test.

959

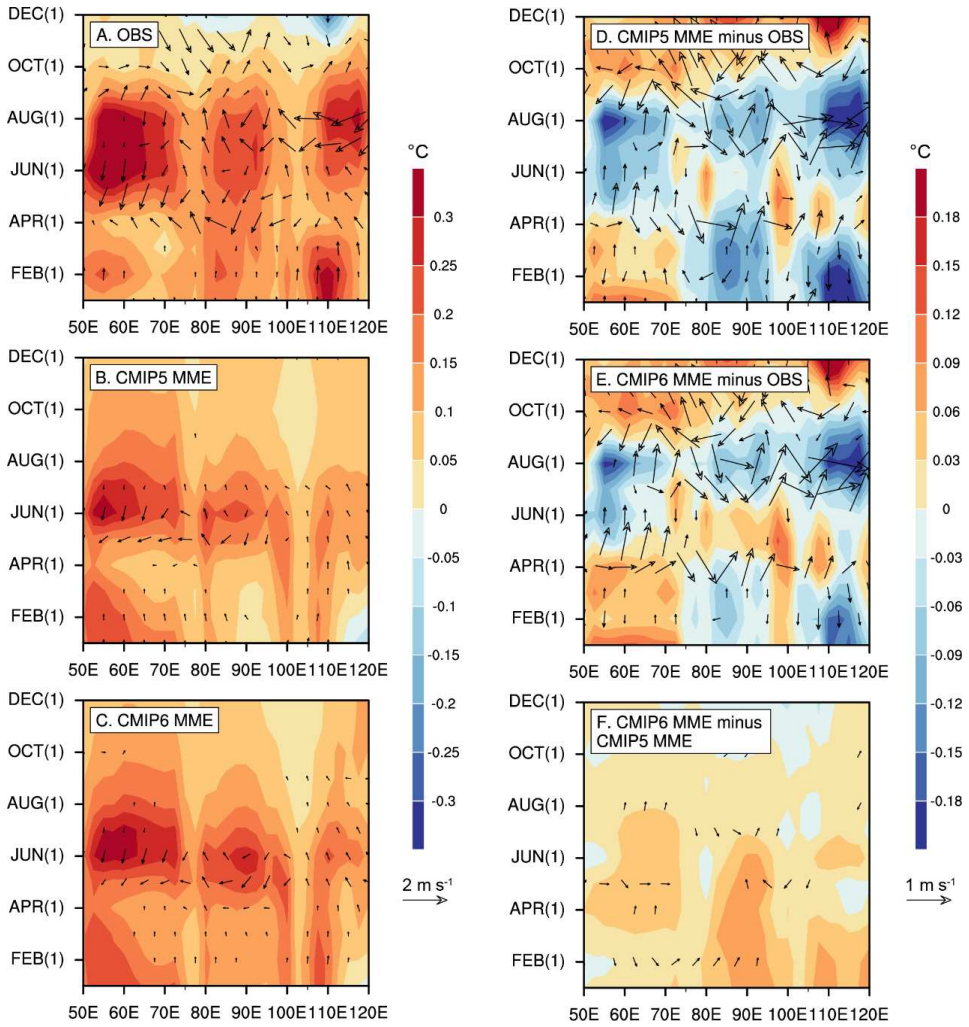

960

961 **Figure 9.** Longitude–time section of 0–20°N averaged SSTA (colors; units: ℃) and 850-hPa wind anomalies
962 (vectors; units: $m\ s^{-1}$) for the El Niño composite in the observation (A), CMIP5 MME (B), CMIP6 MME
963 (C), difference between CMIP5 MME and observation (D), difference between CMIP6 MME and observation
964 (E), and difference between CMIP6 MME and CMIP5 MME (F).

965

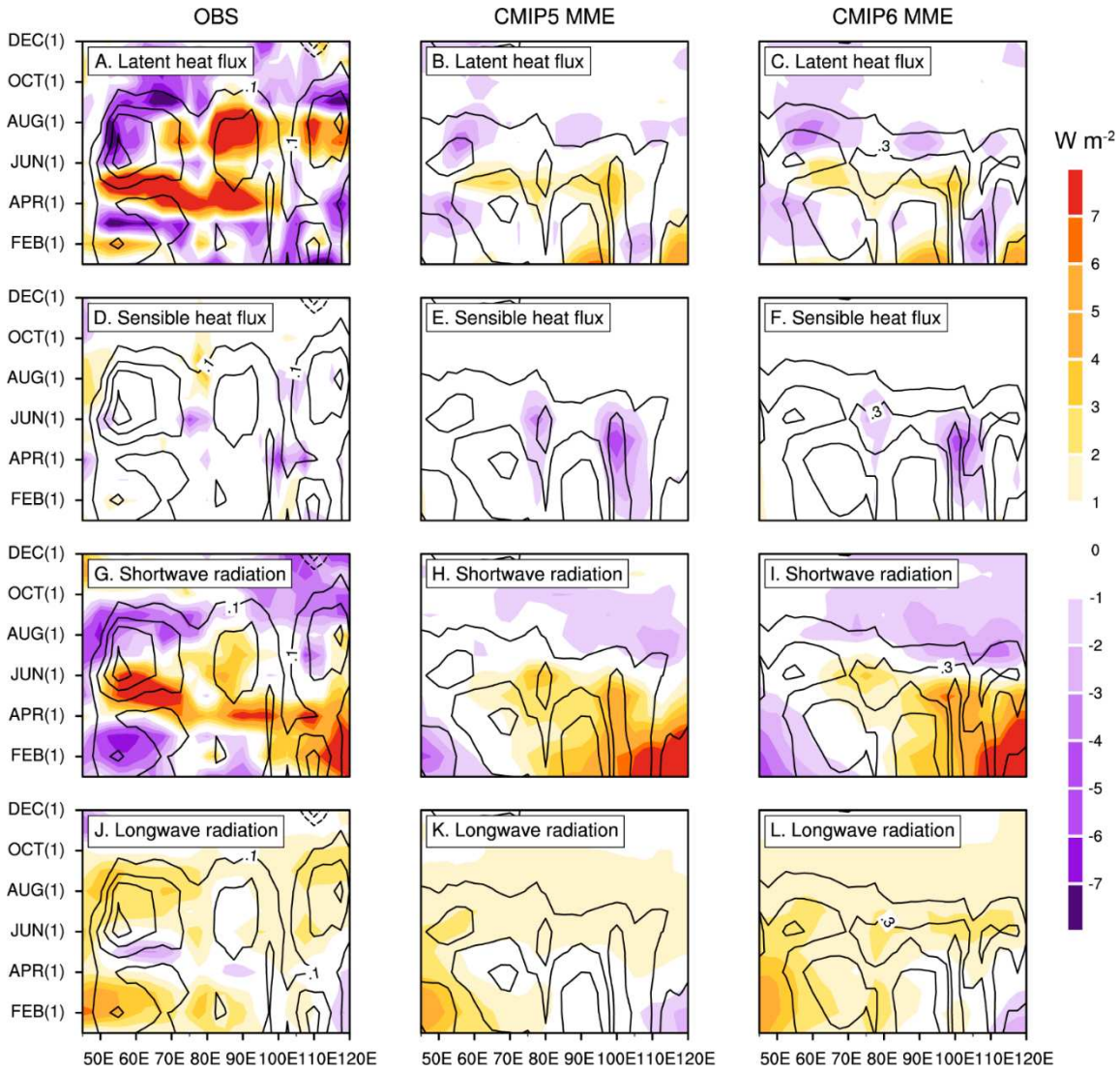

Figure 10. Longitude–time section of 0–20°N averaged SSTA (contours; units: ℃), latent heat flux (shading; units: $W\ m^{-2}$), sensible heat flux (shading; units: $W\ m^{-2}$), shortwave radiation (shading; units: $W\ m^{-2}$), and longwave radiation (shading; units: $W\ m^{-2}$) anomalies for the El Niño composite in the observations (left panels), CMIP5 MME (middle panels), and CMIP6 MME (right panels). Solid and dashed contours at interval of 0.1 (±0.1, ±0.2, ±0.3, …) represent heat fluxes into and out of the ocean, respectively.

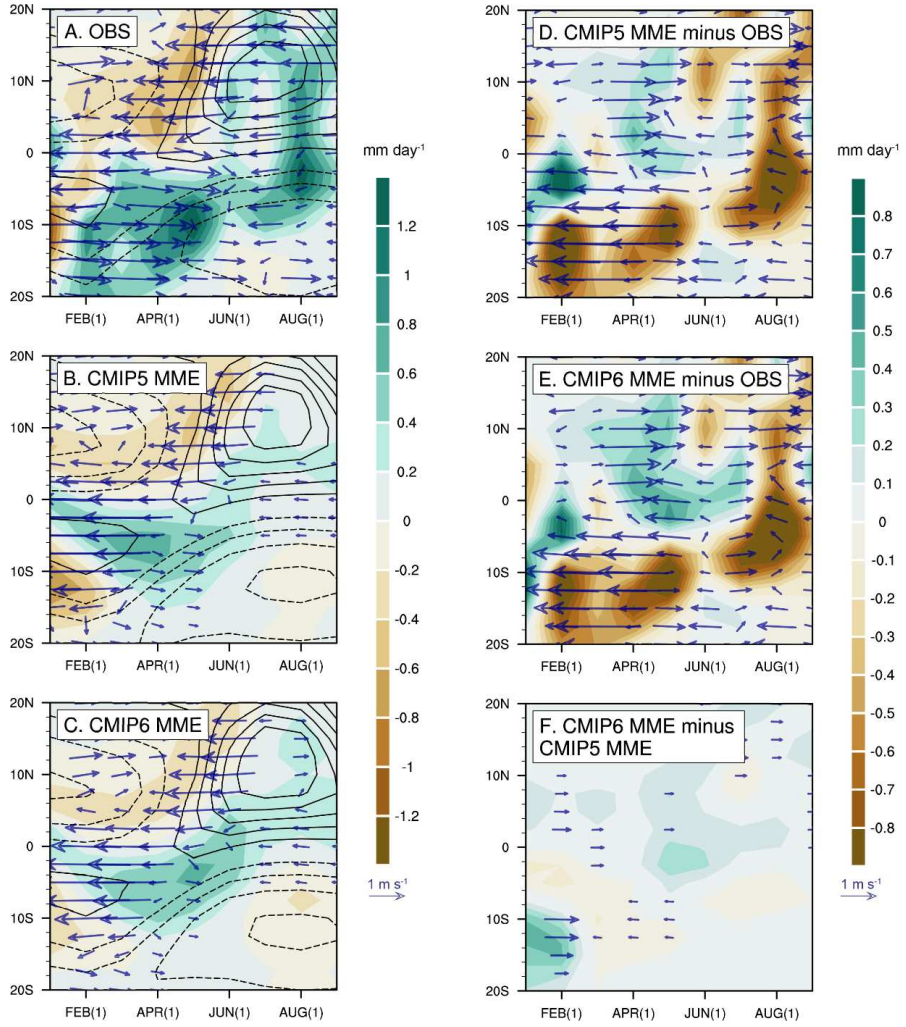

Figure 11. Time–latitude section of 40°–100°E averaged precipitation anomalies (colors; units: $mm\ day^{-1}$) and 850-hPa wind anomalies (vectors; units: $m\ s^{-1}$) for the El Niño composite in the observation (A), CMIP5 MME (B), CMIP6 MME (C), difference between CMIP5 MME and observation (D), difference between CMIP6 MME and observation (E), and difference between CMIP6 MME and CMIP5 MME (F). The black contours in A, B and C denote 850-hPa background zonal wind climatology (interval at $2\ m\ s^{-1}$ with westerly wind by solid contours, easterly wind by dashed contours, and zero omitted).

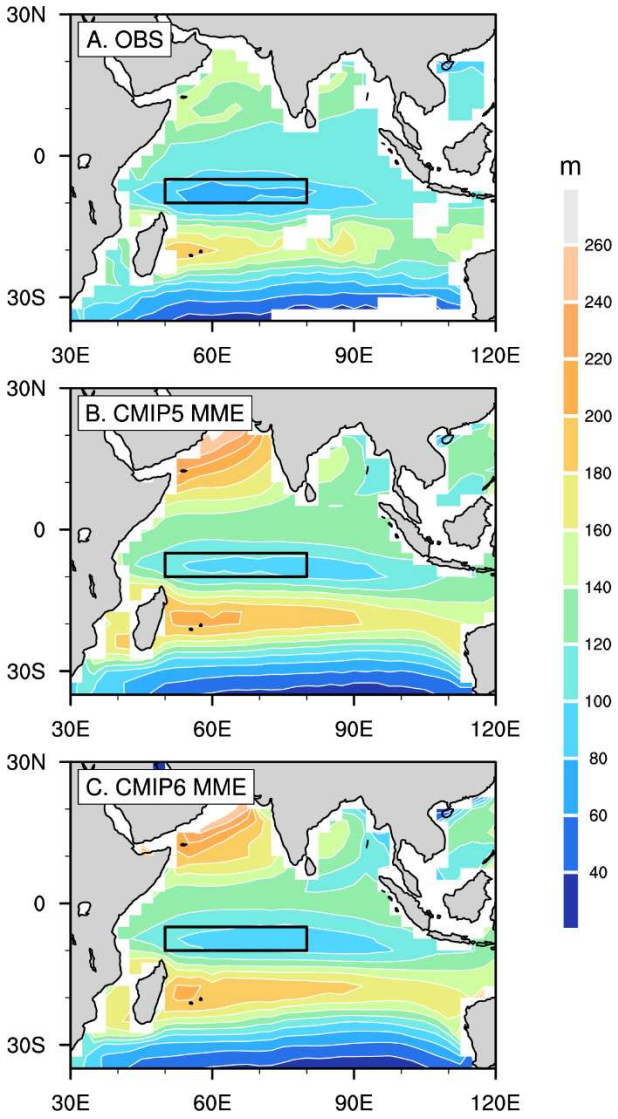

Figure 12. Climatological mean thermocline depth (colors; units: m) in the IO from March to May in the observation (A), CMIP5 MME (B), and CMIP6 MME (C). The SWIO thermocline dome region (10°S–5°S, 50°E–80°E) is highlighted in black box.

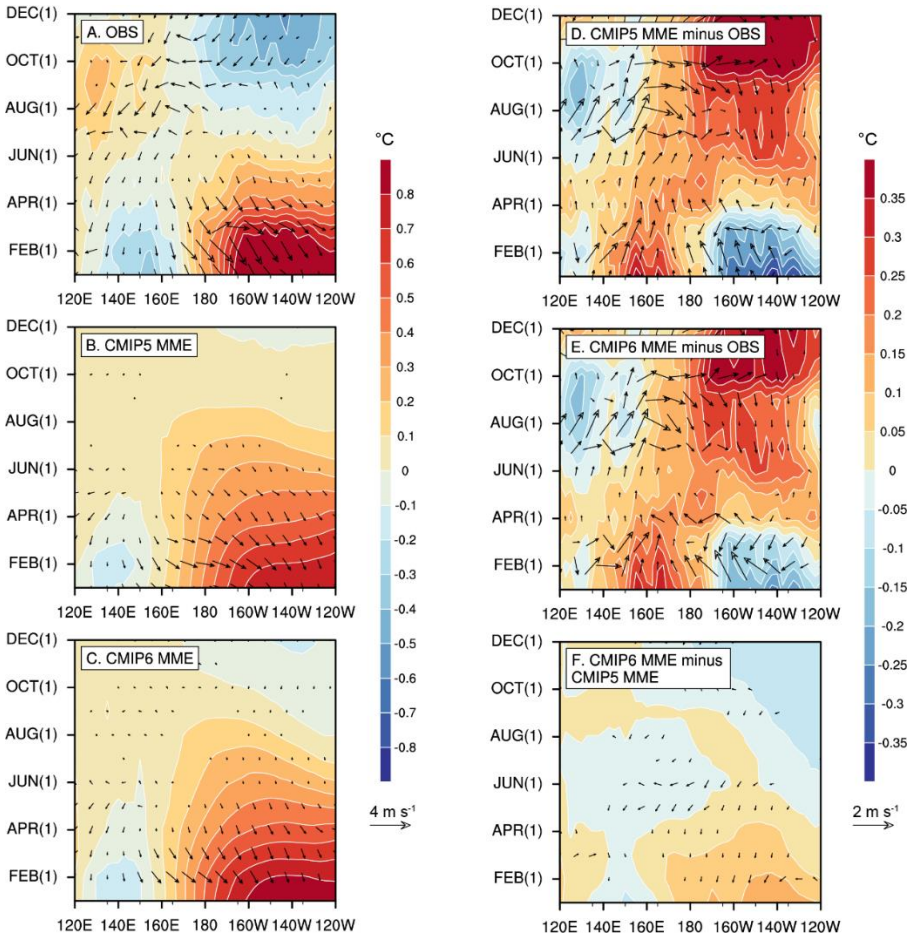

Figure 13. Same as Fig. 9, but for 10°S–10°N averaged anomalies in the Pacific.

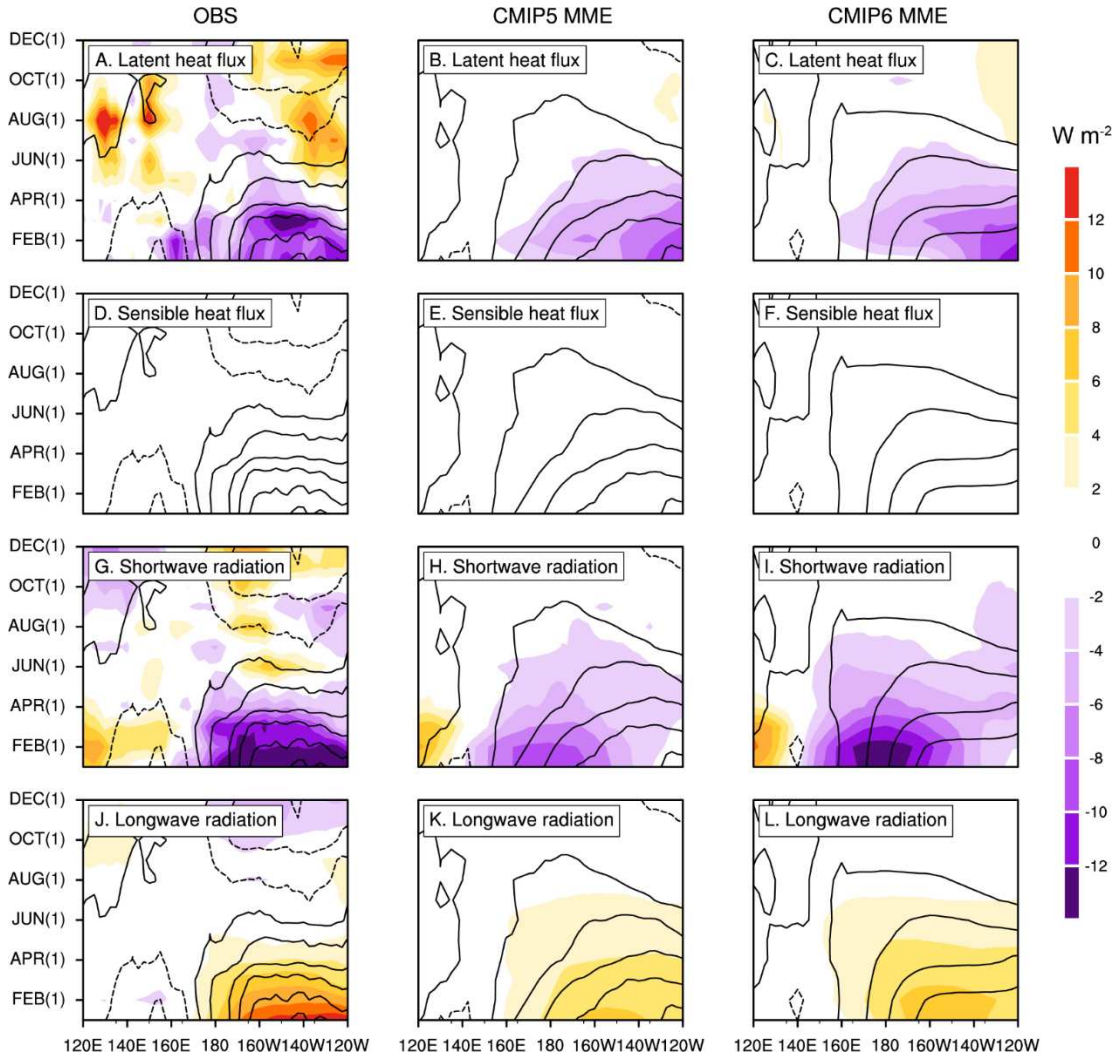

Figure 14. Same as Fig. 10, but for 10°S–10°N averaged anomalies in the Pacific. Solid and dashed contours at interval of 0.2 (±0.1, ±0.3, ±0.5, …) represent heat fluxes into and out of the ocean, respectively.

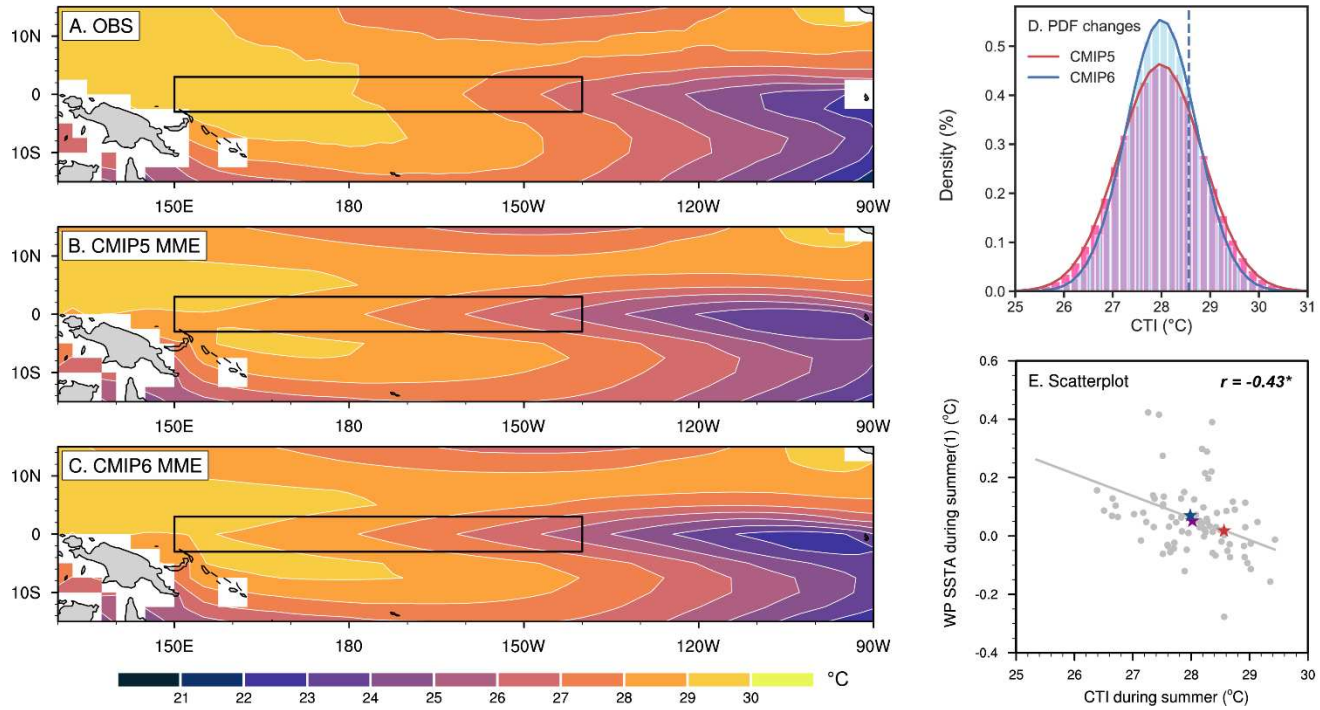

Figure 15. Climatological mean SST (colors; units: ℃) in the tropical Pacific averaged from June to August in the observations (A), CMIP5 MME (B), and CMIP6 MME (C). The cold tongue region (3°S–3°N, 150°E–140°W) is highlighted in black box. The PDFs of CTI (D) for CMIP5 models (red) and CMIP6 models (blue). The dotted blue line denotes the observation. Scatterplot (E) between the climatological mean SST over the equatorial Pacific cold tongue averaged from June to August and El Niño-induced SSTA over WP (10°S–10°N, 140°E–170°W) averaged from June(1) to August(1). The grey solid circles denote CMIP models, while the red, blue and purple stars represent the observations, CMIP5 MME and CMIP6 MME, respectively. The linear regression line and correlation coefficient are shown as well.

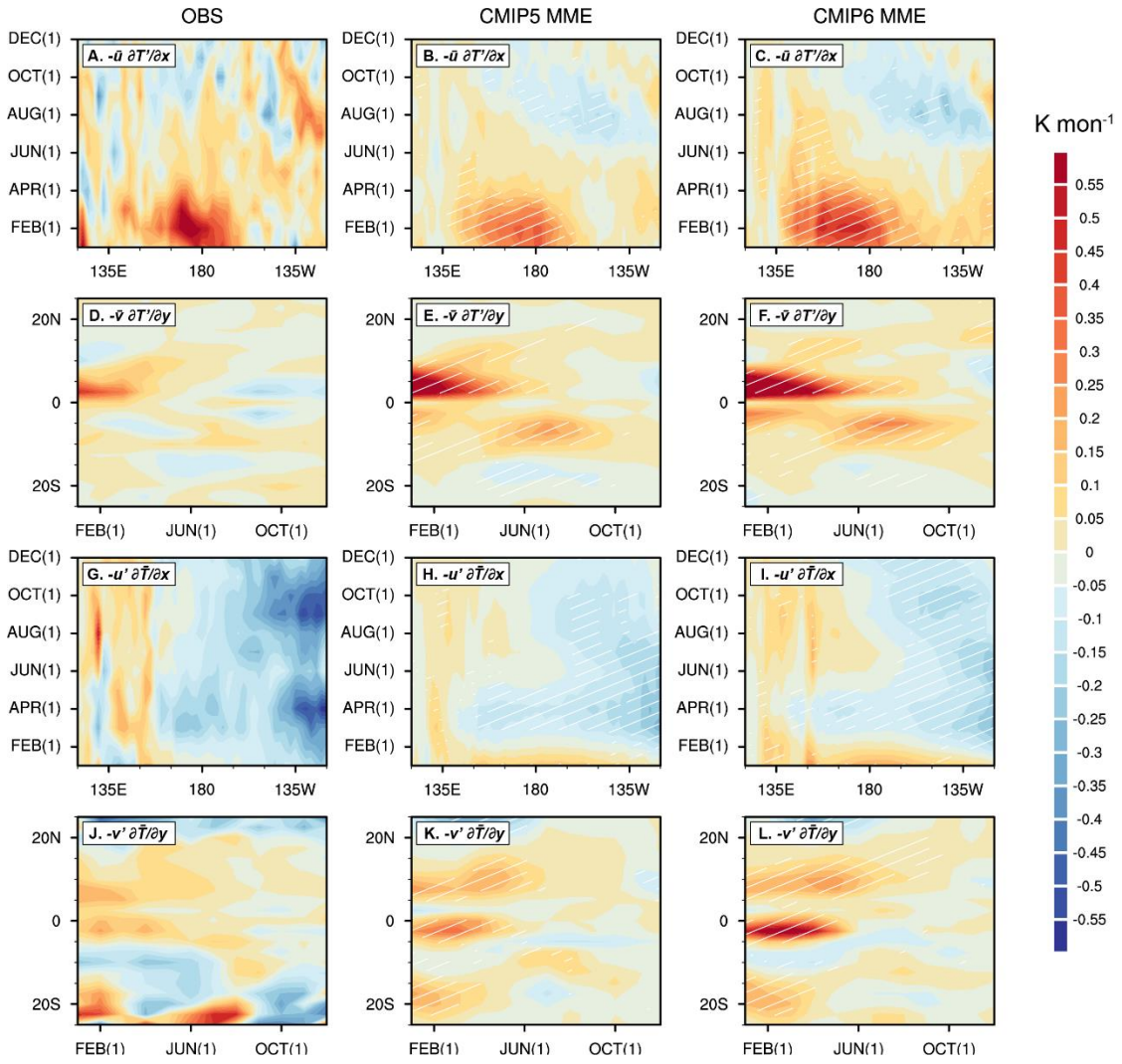

Figure 16. Longitude–time section of 10°S–10°N averaged vertical integrations of mean zonal advection of anomalous potential temperature gradient ($-\bar{u}\,\partial T'/\partial x$; A–C; units: $K\ mon^{-1}$), time–latitude section of 140°–180°E averaged mean meridional advection of anomalous potential temperature gradient ($-\bar{v}\,\partial T'/\partial y$; D–F; units: $K\ mon^{-1}$), longitude–time section of 10°S–10°N averaged anomalous zonal advection of mean potential temperature gradient ($-u'\,\partial \bar{T}/\partial x$; G–I; units: $K\ mon^{-1}$), and time–latitude section of 140°–180°E averaged anomalous meridional advection of mean potential temperature gradient ($-v'\,\partial \bar{T}/\partial y$; J–L; units: $K\ mon^{-1}$) in the ocean mixed layer for the El Niño composite in the observation (left panels), CMIP5 MME (middle panels), and CMIP6 MME (right panels). White hatchings denote that more than 80% of models agree with the sign of the MME (for CMIP models).

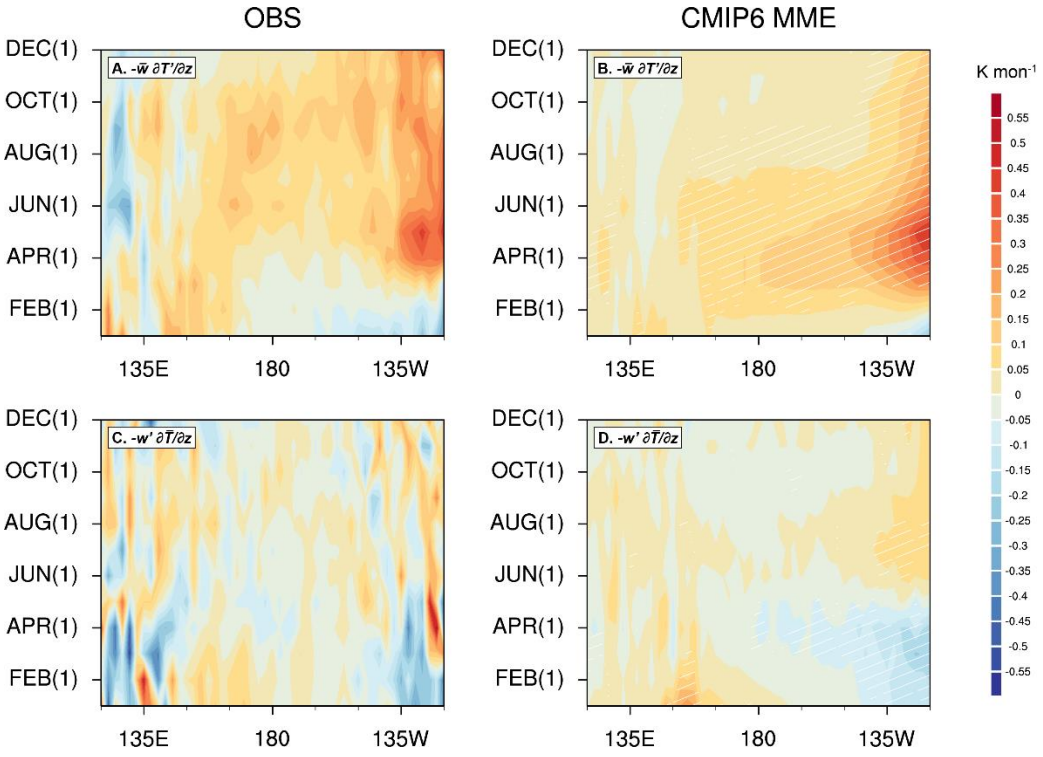

Figure 17. Longitude–time section of 10°S–10°N averaged vertical integrations of thermocline feedback ($-\bar{\omega}\,\partial T'/\partial z$; A–B; units: $K\,mon^{-1}$) and upwelling feedback ($-\omega'\,\partial \bar{T}/\partial z$; C–D; units: $K\,mon^{-1}$) in the ocean mixed layer for the El Niño composite in the observation (left panels) and CMIP6 MME (right panels). White hatchings denote that more than 80% of models agree with the sign of the MME (for CMIP6 models).

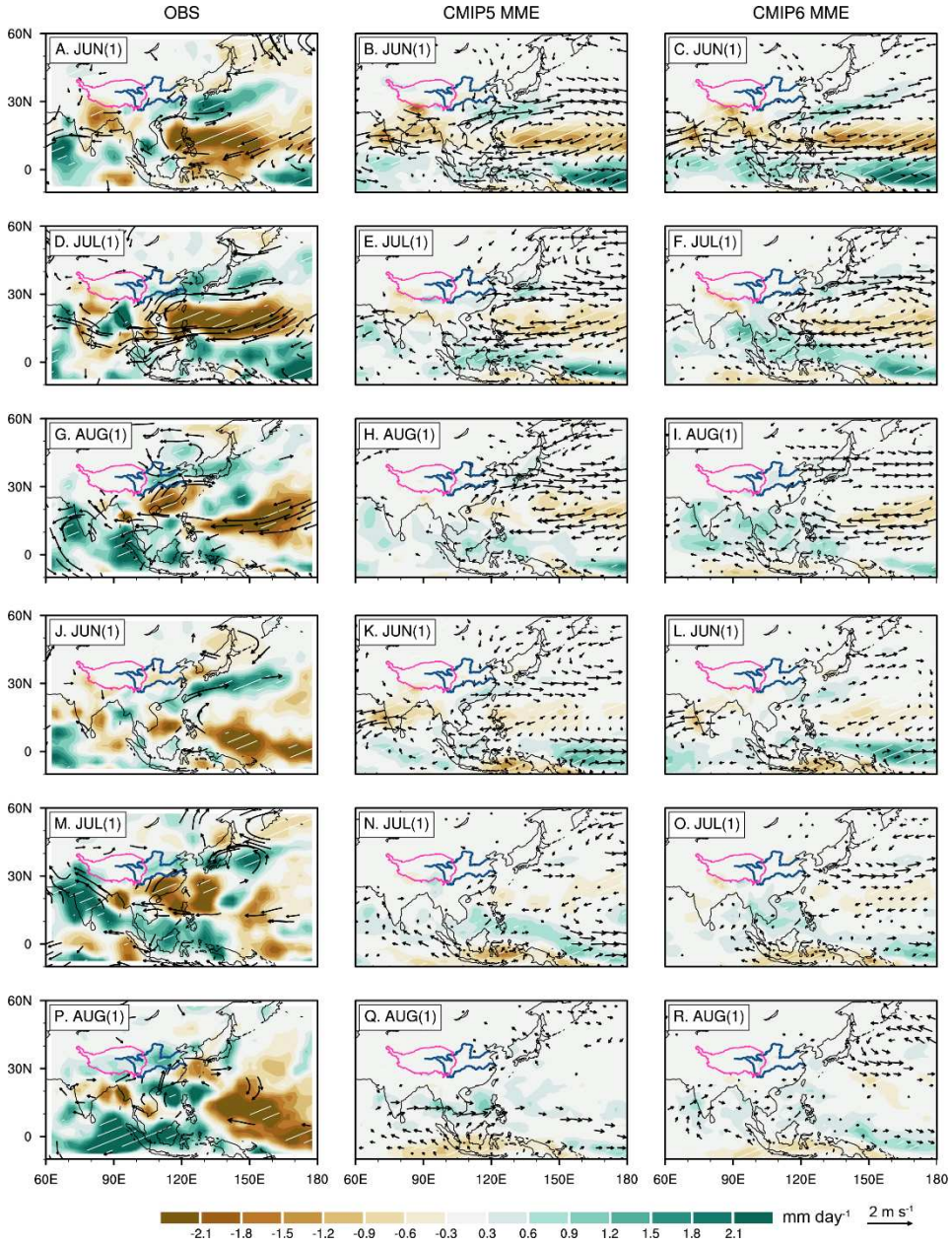

Figure 18. 850-hPa wind (vectors; units: $m\ s^{-1}$) and precipitation (colors; units: $mm\ day^{-1}$) anomalies for the EP (A–I) and CP (J–R) El Niño composite (identified with Niño-3 & Niño-4 index) in the observations (left panels), CMIP5 MME (middle panels), and CMIP6 MME (right panels) during post-El Niño summers. Vectors only exceeding the 95% confidence level are shown. White hatchings denote that the anomalies are significant at the 95% confidence level (for observations) or more than 80% of models agree with the sign of the MME (for CMIP models).

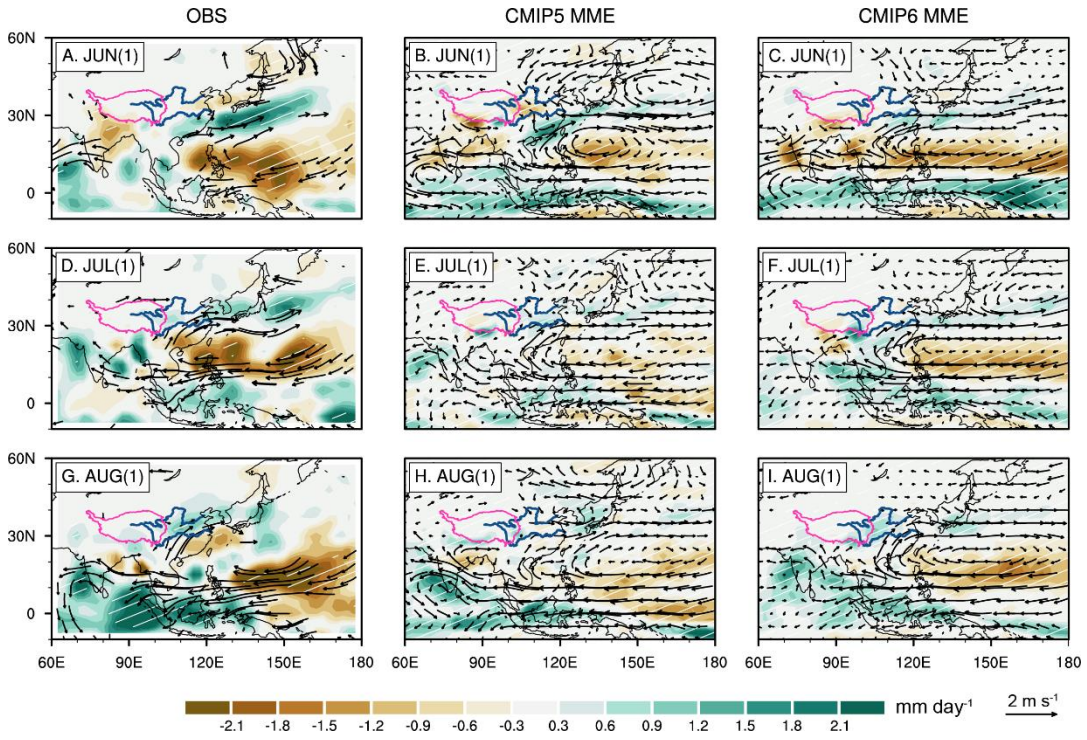

028

029 **Figure 19.** Same as Fig. 1, but for 850-hPa wind (vectors; units: $m\,s^{-1}$) and precipitation (colors; units:

030 $mm\ day^{-1}$) anomalies in high-performance models.

031

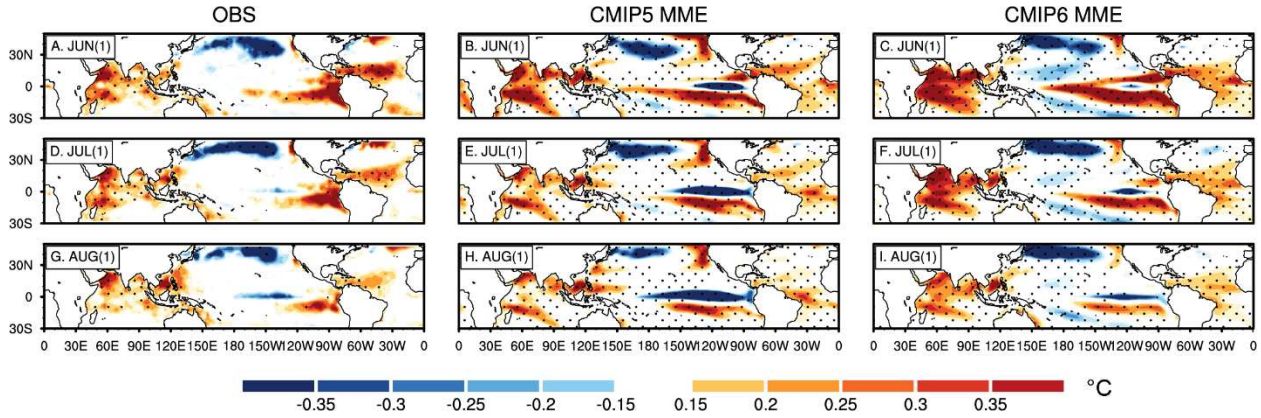

Figure 20. Same as Fig. 4, but for SSTA (colors; units: ℃) in high-performance models.

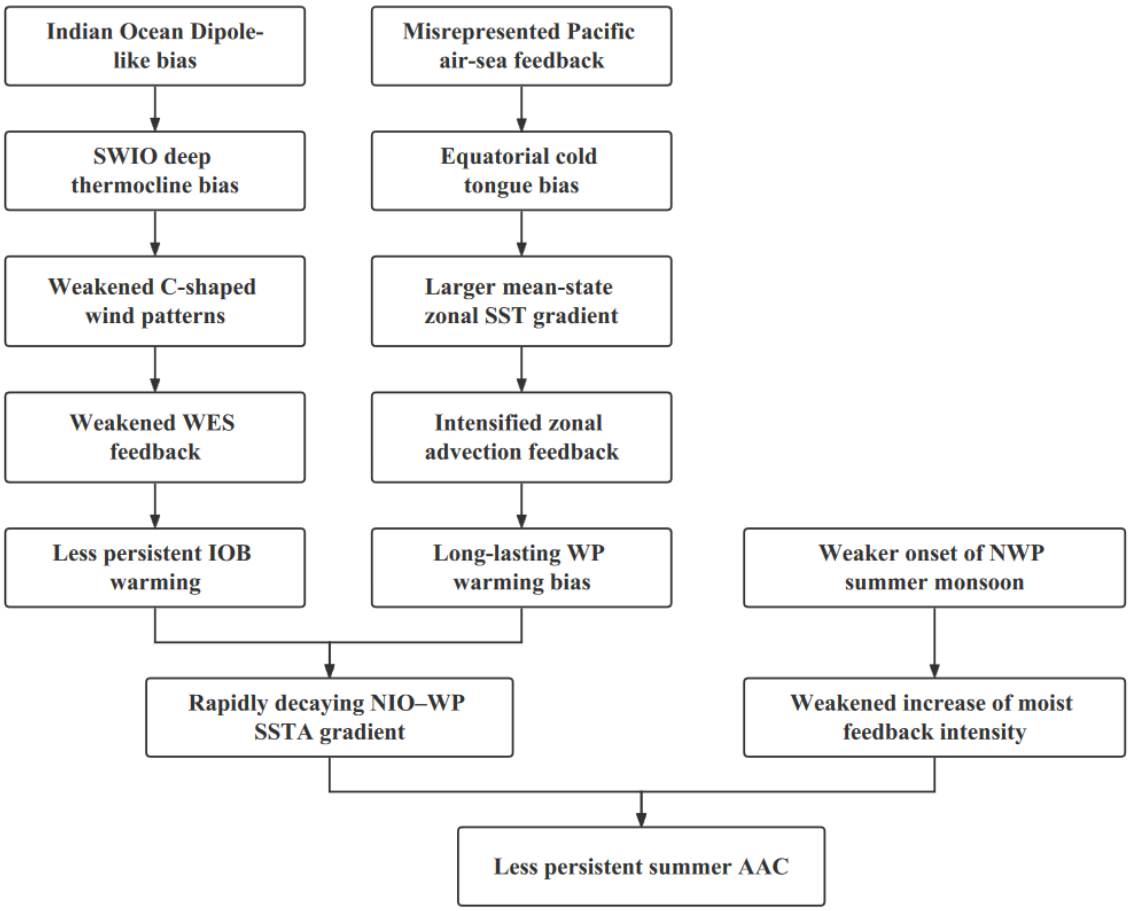

Figure 21. Schematic diagram depicting mechanisms of weak persistence of AAC during post-El Niño summers in CMIP5 and CMIP6 models.